Impact of nonuniform ambient stratification on thermal plume dynamics

Francisco Marques
Departament de Física Aplicada, Universitat Politècnica de Catalunya, Barcelona 08034, Spain

Juan M. Lopez*
School of Mathematical and Statistical Sciences, Arizona State University, Tempe, Arizona 85287, USA

(Received 21 September 2022; accepted 15 February 2023; published 27 February 2023)

Thermal plumes arising from localized buoyancy sources are very common in nature and industrial settings. They have been extensively studied experimentally, theoretically, and numerically, mostly focusing on entrainment and mixing processes in fully developed turbulent regimes. Here, we focus on the primary instabilities of laminar plumes and their transitions as the strength of the buoyancy source (quantified by a Rayleigh number) is increased. Numerous prior studies in this transitional regime have reported a myriad of disparate spatiotemporal plume characteristics. We show that this wide variety of behavior is tied to the various ways an $O(2)$ axisymmetric system can undergo symmetry breaking. Our equivariant dynamical systems theory analyzing the breaking of $O(2)$ symmetry accounts for the spatiotemporal characteristics of the plumes we compute solving the Navier–Stokes–Boussinesq equations. We find that the nature of the ambient stratification plays an important role in determining how $O(2)$ symmetry is broken with increasing Rayleigh number, and this in turn determines the details of the plume spatiotemporal characteristics.

DOI: 10.1103/PhysRevFluids.8.023903

I. INTRODUCTION

Plumes generated by localized buoyancy sources occur naturally in many geophysical settings (e.g., hydrothermal plumes, plumes under ice sheets, firewhirls), as well as in industrial processes. Most of the studies on thermal plumes have focused on the entrainment and mixing properties of fully turbulent plumes [see, for example, the review articles 1–3]. For the most part, interpretation of plume observations and measurements has focused on using the plume model of Morton, Taylor, and Turner [4] and various extensions, which continue to be extensively and productively used for turbulent stratified plume studies [e.g., Ref. 5]. There have been comparatively few studies addressing the transition from steady to unsteady plume regimes, and a general understanding of these processes is still lacking. Such models are not designed to address transition processes, they are designed to model the mean features of fully turbulent plumes. It is a one-dimensional self-similar model of a plume, in the limit of zero viscosity and zero diffusivity, ensemble averaged in time and the horizontal. It models the "mean" plume while the three-dimensional unsteady (turbulent) fluctations are lumped into an entrainment parameter (whose value is determined empirically on a case-by-case basis). There are many aspects of transitional plumes (further detailed below) which are not accessible in such models, such as time-periodic puffing (the model is steady), various three-dimensional unsteady fluctuations (their contributions are lumped into the single entrainment parameter) and the spontaneous generation of swirl (the model assumes an axisymmetric mean velocity with zero

*jmlopez@asu.edu

 ©2023 American Physical Society

swirl). The question of how is swirl spontaneously generated in plumes is particularly pertinent in firewhirls. Even in well-controlled axisymmetric experimental setups, intense swirl is observed in plumes under certain conditions [6]. In natural settings, asymmetries are always present and the swirl is viewed as being due to extraneously imposed symmetry breaking [7], while other studies impose swirl directly at the plume source [8–10] or impose a background rotation [11,12], but there remain many open questions regarding swirling plumes. The review article of Williams [13] concludes that significant unknowns remain about firewhirls, and that although some governing parameters are known, for some types of firewhirls these are not very important and the dominant parameters remain to be discovered. It is our premise that understanding the spontaneous generation of swirl in plumes is an important missing ingredient in a more complete physical picture of buoyant plumes, and in this paper we highlight the role of ambient stratification on this. Most studies of stratified plumes are idealized with a linear ambient stratification, but many natural settings have nonlinear stratification, for example, the pycnocline in the ocean, and there are some studies that take this into account when studying buoyant plumes from a localized source [14].

There continues to be much interest in the transition processes from a steady laminar plume to a turbulent plume. Some relevant questions to be explored are: What are the destabilizing mechanisms? What is the role of symmetries? What are the mechanisms responsible for the generation of swirl? Experimental studies that focus on transition report that the first stages of the transition involve instabilities that introduce unsteadiness and break the circular symmetry of the plume as certain control parameters are varied, but the picture is not coherent with several different scenarios being reported depending on the details of the setup. This is not surprising as the breaking of circular symmetry typically results in a myriad of different dynamical states [15]. If the primary instability of the plume results in unsteadiness while retaining the circular symmetry, then a so-called puffing plume results. These have been observed in some experiments and are commonly found when simulations are restricted to being axisymmetric [16–21]. Other studies (both experimental and numerical) report on nonaxisymmetric primary instabilities leading to so-called wobbling, meandering or buckling plumes [22–25] or swirling plumes [26–29]. The wobbling and swirling plumes break one or other component of the circular symmetry. The wobbling (meandering or buckling) plume has the invariance to arbitrary rotations about its axis broken while retaining the reflection about a meridional plane. However, the swirling plume has broken the meridional reflection, and the rotation component of the circular symmetry results in the spontaneous generation of swirl. Subsequent instabilities lead to complex interactions, and it is unclear if these have been fully reconciled. Part of the problem is that the various dynamic scenarios associated with the breaking of circular symmetry depend on the parameters of the system. These parameters include those describing the geometry and boundary conditions of the system, material properties (viscosities and diffusivities) of the fluid, and buoyancy distributions.

Inspired by the enclosed cylinder experiments of Torrance [27,30,31], where a plume was driven by a localized hot spot on the bottom endwall and the ambient was either of a uniform temperature or a stable linear stratification, Lopez and Marques [32] and Marques and Lopez [33] analyzed the transition processes in thermal plumes in an isothermal ambient and in a stratified ambient, respectively. In Lopez and Marques [32], the ambient was not stratified and first bifurcation led to the axisymmetric puffing plume. With increasing relative temperature of the hot spot (quantified by the Rayleigh number), the plume collides rapidly with the top endwall, leading to complex three-dimensional flows. However, in Marques and Lopez [33] the whole ambient was linearly stratified, the first bifurcation was to a rotating wave state, and puffing sets in as a secondary instability modulating the rotating wave. These two types of ambients differ in which component of the circular symmetry breaks first. To further explore the influence of the ambient on the plume dynamics, we consider here a partially stratified ambient, similar to that used by Ansong and Sutherland [34], but using temperature rather than salt stratification. The study of Ansong and Sutherland [34] examined properties of axisymmetric waves emanating from a plume impinging upon a stratified fluid, and their idealized system was motivated by the aim to isolate the dynamics of the mechanical oscillator effect acting within a convective storm. In this setup, the bottom half

of the ambient is at a uniform temperature (that of the bottom endwall outside of the hot spot in its center), and the top half of the ambient is linearly stratified with the temperature at the top being that of the hot spot. The dynamics of plumes in this mixed ambient includes aspects from both the isothermal and linearly stratified ambients, which are all tied to the ways that the circular symmetry is broken.

In the present study, the choice of geometry, parameter regimes and ambient stratification is such that the dynamics observed when the ambient is homogeneous [32] and when it is linearly stratified [33], governed by the different ways $O(2)$ symmetry is broken for each case, occur roughly simultaneously with increasing Rayleigh number in the present setup. The use of equivariant dynamical systems theory provides new physical insight in understanding how and why the myriad of different spatiotemporal behaviors observed by many (some are listed above) in a variety of different circumstances come about. The dynamical systems theory is agnostic of any physical application, yet it is able to account for the myriad of plume states and their spatiotemporal characteristics computed from the full nonlinear Navier–Stokes–Boussinesq equations. An important result from the present study is that the nature of the ambient has an important impact on how $O(2)$ symmetry is broken with increasing Rayleigh number, and that in turn has a huge impact on the spatiotemporal characteristics of the plumes.

II. GOVERNING EQUATIONS

Consider the flow in a circular cylinder of radius R and length L, with no-slip boundary conditions, filled with a fluid of constant kinematic viscosity ν, thermal diffusivity κ, and coefficient of thermal expansion α, that is driven by temperature profiles imposed on the cylinder walls. The bottom endwall has a fixed temperature T_0^*, except for a disk of diameter D at its center which is at a hotter temperature T_1^*. The top endwall is kept at the hot disk temperature T_1^*. The sidewall is kept at the temperature T_0^* up to a height H and then the sidewall temperature varies linearly with height between T_0^* at H and T_1^* at the top, resulting in a stable stratification if not for the hot spot at the bottom.

The system is nondimensionalized using the diameter of the hot spot D as the length scale, D^2/κ as the timescale, $\Delta T^* = T_1^* - T_0^*$ as the temperature scale, and $\kappa^2\rho_0/D^2$ as the pressure scale, where ρ_0 is the fluid density at temperature T_0^*. The Boussinesq approximation is implemented, treating all fluid properties as constant except for a linear variation of density with temperature in the gravitational buoyancy term. The nondimensional Navier–Stokes–Boussinesq governing equations are

$$\begin{aligned}(\partial/\partial t + \boldsymbol{u}\cdot\boldsymbol{\nabla})\boldsymbol{u} &= -\boldsymbol{\nabla} p + \mathrm{Pr}\nabla^2\boldsymbol{u} + \mathrm{PrRa}\, T\widehat{\boldsymbol{z}},\\ (\partial/\partial t + \boldsymbol{u}\cdot\boldsymbol{\nabla})T &= \nabla^2 T, \quad \boldsymbol{\nabla}\cdot\boldsymbol{u} = 0,\end{aligned} \tag{1}$$

where $\boldsymbol{u} = (u, v, w)$ is the velocity in cylindrical coordinates $(r, \theta, z) \in [0, a_r] \times [0, 2\pi] \times [0, a_z]$, the corresponding vorticity vector is $\boldsymbol{\omega} = \boldsymbol{\nabla}\times\boldsymbol{u} = (\xi, \eta, \zeta)$, p is the reduced pressure, $\widehat{\boldsymbol{z}} = (0, 0, 1)$ is the unit vector in the vertical z direction and $T = (T^* - T_0^*)/\Delta T^*$ is the nondimensional temperature, while T^* is the dimensional temperature. The nondimensional parameters are:

$$\begin{aligned}\text{Rayleigh number:}\quad & \mathrm{Ra} = \alpha g D^3 \Delta T^*/\kappa\nu,\\ \text{Prandtl number:}\quad & \mathrm{Pr} = \nu/\kappa,\\ \text{radial aspect ratio:}\quad & a_r = R/D,\\ \text{axial aspect ratio:}\quad & a_z = L/D,\\ \text{stratification level:}\quad & a_s = H/D,\end{aligned} \tag{2}$$

where g is the acceleration due to gravity. Often, a Grashof number is used instead of the Rayleigh number, but these are related by $\mathrm{Gr} = \mathrm{Ra}/\mathrm{Pr}$. In the present study, the Prandtl number is fixed

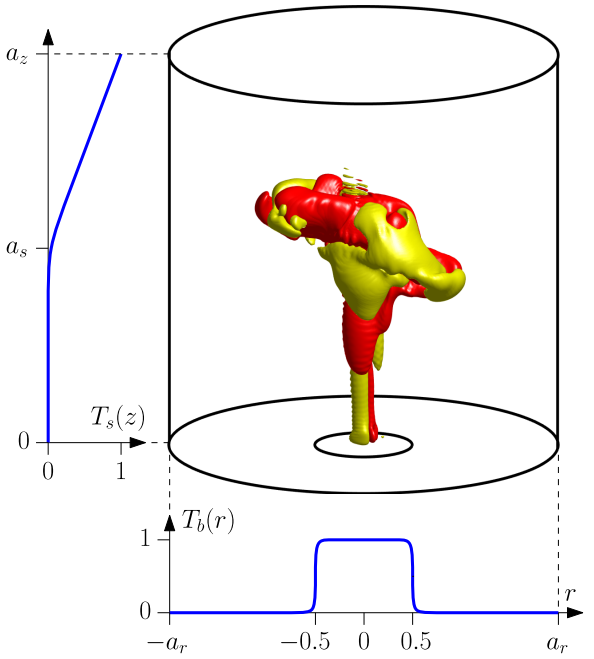

FIG. 1. Schematic of the cylindrical container with a hot spot at the center of the bottom endwall. The geometric parameters are $a_r = 2$, $a_z = 4$, $a_s = 2$. Shown are isosurfaces of helicity density for a plume at $\mathrm{Ra} = 3 \times 10^6$; the isosurface levels are $\mathrm{he} = \pm 1.1 \times 10^4$.

at $\mathrm{Pr} = 7$, which is the value for water nominally at room temperature. We use a Rayleigh number based on the hot spot diameter D, as is typically done in natural convection problems due to localized heating [27], rather than a dimension of the container. Another useful quantity is the helicity density, $\mathrm{he} = \boldsymbol{u} \cdot \boldsymbol{\omega}$, the scalar product of the velocity and vorticity fields.

The boundary conditions for velocity at the cylinder walls are no-slip, $\boldsymbol{u} = \boldsymbol{0}$. The temperature is imposed at the walls as

$$\begin{aligned} \text{top } z = a_z: &\quad T = 1, \\ \text{sidewall } r = a_r: &\quad T = T_s(z) = \begin{cases} 0 & z \in [0, a_s], \\ (z - a_s)/(a_z - a_s) & z \in [a_s, a_z], \end{cases} \\ \text{bottom } z = 0: &\quad T = T_b(r) = \begin{cases} 1 & r \in [0, 1/2), \\ 0 & r \in (1/2, a_r]. \end{cases} \end{aligned} \tag{3}$$

$T_b(r)$ is discontinuous at $r = 1/2$, and T_s has a discontinuous z derivative at $z = a_s$. To improve the spectral convergence of the numerical scheme, and also to mimic real boundary conditions where there are no discontinuities, we have regularized the temperature profiles at the walls:

$$T_b(r) = 0.5[1 - \tanh c_b(r - 0.5)], \quad r \in [0, a_r], \tag{4}$$

$$dT_s(z)/dz = 0.5(a_z - a_s)^{-1}[1 + \tanh c_s(z - a_s)], \quad z \in [0, a_z]. \tag{5}$$

The parameters c_b and c_s fix the width of the regularization regions. We have chosen $c_b = 11.1$ and $c_s = c_b\, a_r/a_z$, for which there are a reasonable number of collocation points over the regularization interval. This choice coincides with the hot spot regularization used in Lopez and Marques [32] and Marques and Lopez [33]. The schematic of the setup in Fig. 1 also includes plots of the regularized wall temperature profiles used.

The fluid density is given by $\rho^*(z^*) = \rho_0[1 - \alpha(T^*(z^*) - T_0^*)]$. In the absence of the hot spot, the governing equations admit a solution with $\boldsymbol{u} = \boldsymbol{0}$ and a stable temperature stratification $T(z) = T_s(z)$. In the region where the stratification is linear, $z \in [a_s, a_z]$, the fluid can support internal gravity waves. The buoyancy frequency in the initially linearly stratified upper region is

$$N = \sqrt{-\frac{g}{\rho_0}\frac{d\rho^*}{dz^*}} = \sqrt{\frac{\alpha g \Delta T^*}{(L-H)}}, \tag{6}$$

which can be nondimensionalized by the thermal timescale to define a buoyancy number

$$R_N = \frac{ND^2}{\kappa} = \sqrt{\frac{\mathrm{PrRa}}{(a_z - a_s)}}. \tag{7}$$

Frequencies of states computed using the thermal timescale can be converted to the buoyancy timescale by dividing by R_N; the arcsin of such frequencies determines the inclination with respect to gravity of the internal waves in regions of constant N.

A. Numerical technique

The same spectral collocation method that was used in Lopez and Marques [32] and Marques and Lopez [33] is used here. It employs a second-order time-splitting method together with a Galerkin–Fourier expansion in θ and Chebyshev collocation in r and z. The expansions for the velocity components and temperature (u, v, w, T) are given by the real part of

$$F(r, \theta, z, t) = \sum_{m=0}^{2n_r+1} \sum_{n=0}^{n_z} \sum_{k=-n_\theta/2}^{n_\theta/2-1} F_{mnk}(t)\Xi_m(r/a_r)\Xi_n(2z/a_z - 1)e^{ik\theta}, \tag{8}$$

where F is any of u, v, w, or T, and Ξ_j is the jth Chebyshev polynomial. Using the prescription in Fornberg [35], the coefficients are such that $u_{mnk} = v_{mnk} = 0$ for $k + m$ even and $w_{mnk} = T_{mnk} = 0$ for $k + m$ odd. In this way, there are no collocation points on the axis (thereby avoiding the polar coordinate singularity at the axis), and the governing equations are solved in the physical domain. The combinations $u_\pm = u \pm iv$ are used to decouple the linear diffusion terms in the momentum equations. Then, for each Fourier mode, the resulting Helmholtz equations for u_+, u_-, w, and T are solved using a diagonalization technique in r and z. The code has been extensively tested and verified in a wide variety of enclosed cylinder flows, and in particular our prior related studies of plumes [32,33]. For the parameter regimes considered in the present study, $n_r = n_z = 150$ Chebyshev modes in the radial and axial directions and $n_\theta = 36$ azimuthal Fourier modes are used, along with time step $\delta t = 10^{-6}$.

B. Symmetries

The governing equations and boundary conditions have circular $O(2)$ symmetry, that is, they are invariant under arbitrary rotations around the cylinder axis and reflections about meridional planes. The actions of the rotations and reflections on the velocity, temperature, vorticity and helicity density, $\mathrm{he} = \boldsymbol{u} \cdot \boldsymbol{\omega}$, are

$$\begin{aligned} &\mathcal{R}_\alpha{:}[u, v, w, T, \xi, \eta, \zeta, \mathrm{he}](r, \theta, z, t) \mapsto [u, v, w, T, \xi, \eta, \zeta, \mathrm{he}](r, \theta - \alpha, z, t), \\ &\mathcal{K}_0{:}[u, v, w, T, \xi, \eta, \zeta, \mathrm{he}](r, \theta, z, t) \mapsto [u, -v, w, T, -\xi, \eta, -\zeta, -\mathrm{he}](r, -\theta, z, t), \end{aligned} \tag{9}$$

where α is an arbitrary angle. $\mathcal{R}_\alpha$ is the rotation by angle α about the cylinder axis; rotations generate the group $SO(2)$. $\mathcal{K}_0$ is the reflection about the meridional plane $\theta = 0$; the reflection about any other meridional plane $\theta = \alpha$ is obtained by combining $\mathcal{K}_0$ with the rotation $\mathcal{R}_\alpha$, i.e., $\mathcal{K}_\alpha = \mathcal{K}_0\mathcal{R}_\alpha$. Since $\mathcal{K}_0^2$ is the identity, it generates the group Z_2. $\mathcal{R}_\alpha$ and $\mathcal{K}_0$ do not commute ($\mathcal{K}_0\,\mathcal{R}_\alpha = \mathcal{R}_{-\alpha}\,\mathcal{K}_0$), and

together they generate the group $O(2) = SO(2) \rtimes Z_2$ (semidirect product) acting on the periodic azimuthal θ-direction; see Marques and Lopez [33] for more details.

Axisymmetric solutions to (1) may be either $SO(2)$ or $O(2)$ invariant. The velocity of an axisymmetric solution, for which $\partial/\partial\theta = 0$, may be decomposed into its meridional and azimuthal components,

$$\boldsymbol{u}(r, z, t) = (u, 0, w) + (0, v, 0). \tag{10}$$

If $v = 0$, then $\boldsymbol{u}$ is purely meridional and $O(2)$ invariant, whereas if the azimuthal component v is nonzero, then $\boldsymbol{u}$ is swirling and only $SO(2)$ invariant. The vorticity for an axisymmetric $\boldsymbol{u}$ can also be decomposed into its meridional and azimuthal components

$$\boldsymbol{\omega} = (\xi, 0, \zeta) + (0, \eta, 0), \tag{11}$$

where the azimuthal component $\eta = \partial u/\partial z - \partial w/\partial r$ only depends on the meridional components of velocity, and the meridional components $r\xi = -\partial(rv)/\partial z$ and $r\zeta = \partial(rv)/\partial r$ only depend on the azimuthal component of velocity. If $v = 0$, i.e., $\boldsymbol{u}$ is $O(2)$ invariant, then the meridional component of $\boldsymbol{\omega}$ is zero, and so the velocity and vorticity are orthogonal and the helicity density $\mathrm{he} = (u, 0, w)\cdot(0, \eta, 0) = 0$, whereas for $SO(2)$ invariant solutions, $\mathrm{he} \neq 0$. Solutions which are not axisymmetric ($\partial/\partial\theta \neq 0$) have broken $\mathcal{R}_\alpha$ (with $\alpha \neq 0$). If such solutions retain $\mathcal{K}_\beta$ invariance (for a specific β), then their helicity is zero, $\mathrm{He} = 0$. The helicity is the volume integral of the helicity density, a convenient measure of the swirl of the solution considered:

$$\mathrm{He} = \int_{\mathcal{D}} \mathrm{he}\, \mathrm{d}\mathcal{V}. \tag{12}$$

However, even when the helicity He is zero, the L_2 norm of the helicity density, $\|\mathrm{he}\|_2$, may be nonzero, where

$$\|\mathrm{he}\|_2 = \left[\int_{\mathcal{D}} \mathrm{he}^2\, \mathrm{d}\mathcal{V}\right]^{1/2}. \tag{13}$$

Careful consideration of the symmetries of the computed flows is found to be essential in disentangling the myriad of coexisting flow states.

III. THE $O(2)$-SYMMETRIC STEADY BASIC STATE

The basic states when the ambient temperature is either uniform or linearly stratified have been described over several ranges of the governing parameters in Lopez and Marques [32] and Marques and Lopez [33]. In this section, we simply compare the basic states in a single geometry with aspect ratios $a_r = 2$ and $a_z = 4$, and also fix $\mathrm{Pr} = 7$ and $\mathrm{Ra} = 2.5 \times 10^5$. Under these conditions, basic states are stable in the three different ambient conditions: (i) uniform with $T(a_r, z) = 1$ and $a_s = a_z$, (ii) mixed with $a_s = a_z/2$, and (iii) linearly stratified with $T(a_r, z) = z$ and $a_s = 0$ in Eq. (3). In the three cases, $a_r = 2$ and $a_z = 4$. Figure 2 shows the isotherms in a meridional plane and isosurfaces of the azimuthal component of vorticity (the only nonzero component of vorticity in the $O(2)$-symmetric basic states), for the three cases. Near the hot spot on the bottom, all three plumes are very similar, but they vary significantly with height above the hot spot due to the differences in the ambient conditions. With the isothermal ambient, the plume flows all the way to the top endwall, whereas for the other two stratified conditions, the plume only extends to approximately the neutral buoyancy level, which is higher above the hot spot in the mixed case than it is in the linearly stratified ambient case. How the plume interacts with the top endwall or the neutral buoyancy level greatly affects its stability and subsequent nonlinear dynamics. The mixed ambient case shows dynamic aspects from both of the other two cases, and these are explored in the following sections.

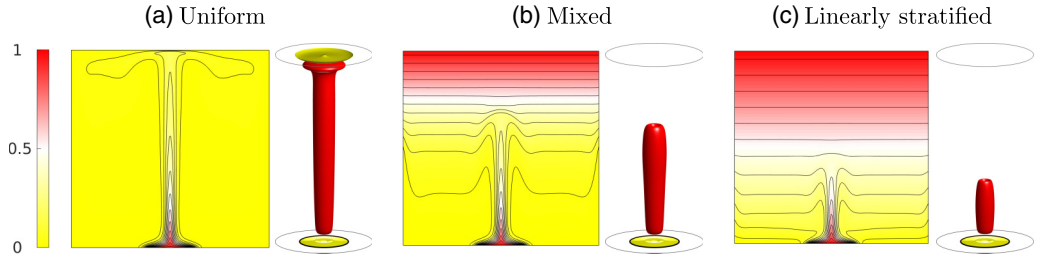

FIG. 2. Basic states corresponding to different ambient temperature profiles, as indicated, at Ra = 2.5×10^5. On the left for each case are the isotherms in the entire meridional plane (i.e., the two planes $(r, z) \in [0, 2] \times [0, 4]$ with $\theta = 0$ and π); the contour levels are equispaced between $T = 0$ (yellow) and $T = 1$ (red), with white corresponding to $T = 0.5$. On the right are azimuthal vorticity isosurfaces at $\eta = \pm 2 \times 10^3$; the gray circles at the top and bottom are drawn at the half radius of the cylinder.

IV. THE $O(2)$-SYMMETRIC PUFFING PLUME, P_0

From now on, we only consider the mixed ambient state with $a_s = 2$. The basic state loses stability via a supercritical Hopf bifurcation to an $O(2)$-symmetric puffing plume at Ra $\approx 2.022 \times 10^6$. Figure 3(a) shows how the oscillation amplitude of the bifurcating limit cycle varies with Ra, using the standard deviation of the kinetic energy, STD$[E]$, as a measure of the oscillation amplitude, where the kinetic energy is

$$E = \frac{1}{2} \int_{\mathcal{D}} \boldsymbol{u} \cdot \boldsymbol{u} \, \mathrm{d}\mathcal{V}. \tag{14}$$

Figure 3(b) shows how its frequency, the puffing frequency, rescaled using the buoyancy timescale, has very little variation with Ra: $\omega_0/R_N \approx 1.48$.

None of the spatial symmetries are broken at the Hopf bifurcation, so the bifurcated state is an $O(2)$-symmetric periodic solution. The instability mechanism is the emission of puffs of warm fluid from the hot spot, so we call these solutions $O(2)$-symmetric puffing plumes, P_0. The generation of the puffs is essentially the same as that described in Lopez and Marques [32] for the primary instability of the localized plume in a nonstratified ambient as their generation is at the base of the hot spot, which is in the lower nonstratified ambient irrespective of the stratification of the upper ambient. The difference in the present problem is that when the puff reaches the neutral buoyancy level it overshoots slightly and bounces back. In the bounce-back process, the azimuthal vorticity of the puff (the only nonzero component of vorticity for an $O(2)$-symmetric state) changes sign. As the next puff approaches the neutral buoyancy level, it collides with the remnants of the previous puff that is still sinking, absorbing it, and then the process repeats. This can be clearly seen in Fig. 4,

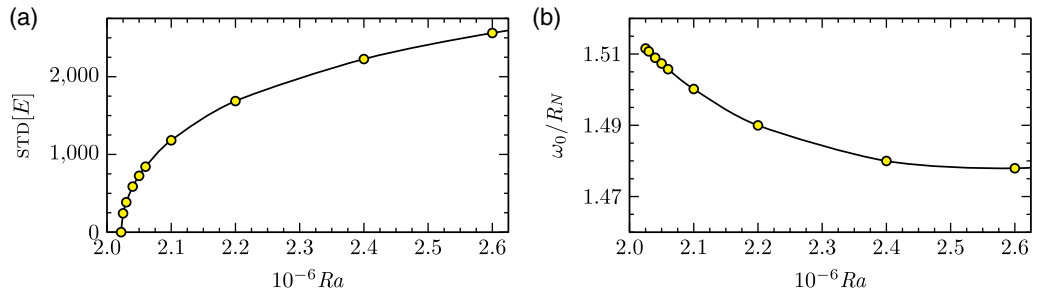

FIG. 3. Variations with Ra of (a) the standard deviation of the kinetic energy, STD$[E]$, and (b) frequency, ω_0/R_N, of the $O(2)$-symmetric periodic puffing plumes, P_0.

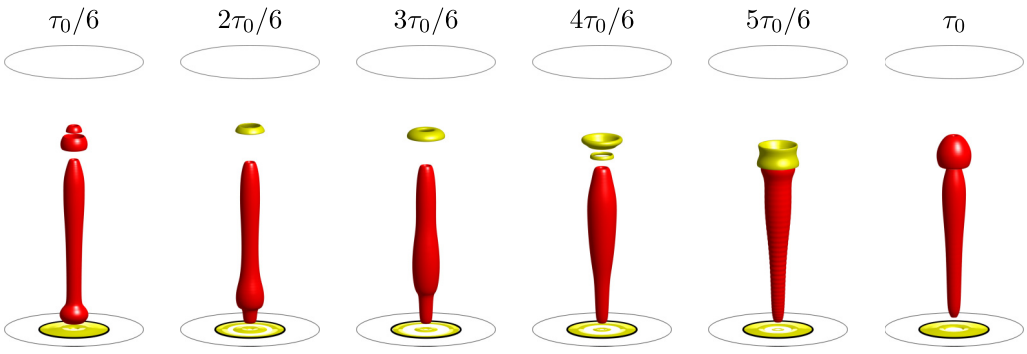

FIG. 4. Snapshots of the the azimuthal vorticity, η, of the $O(2)$-symmetric puffing plume, P_0, at Ra $= 2.60 \times 10^6$ over one puffing period, $\tau_0 = 2\pi/\omega_0$, with $\omega_0/R_N \approx 1.48$. The isosurface levels are $\eta = 10^4$ (red) and $\eta = -8 \times 10^3$ (yellow). The black circle is the hot spot, and the gray circles are on the top and bottom lids at midradius.

showing snapshots of the azimuthal vorticity, η, of P_0 at Ra $= 2.60 \times 10^6$ over a puffing period $\tau_0 = 2\pi/\omega_0 \approx 0.00142$, with $\omega_0/R_N \approx 1.48$. Close inspection of the snapshot at $5\tau_0/6$ shows evidence of a wavy disturbance along the plume. These are reminiscent of the short-lived internal waves on thermal plumes reported by Vincent *et al.* [36], but may also be due to marginal resolution of the solution associated with the large local vertical temperature gradients following the collision between the current puff and the receding prior puff. In Appendix A, the puffing plume at Ra $= 2.60 \times 10^6$ with the current spatial and temporal resolution is compared with that using twice the resolution. While the current resolution is marginal, it is in the converged regime.

V. INSTABILITY OF THE $O(2)$-SYMMETRIC PUFFING PLUME

The axisymmetric puffing plume P_0 loses stability at Ra$_c \approx 2.62 \times 10^6$ via a symmetry-breaking bifurcation, and the bifurcating flows have nonzero helicity density. In Fig. 5, the time-average of the L_2 norm of the helicity density, $\langle \|\mathrm{he}\|_2 \rangle$, is used as a measure of the state's amplitude to illustrate the bifurcation diagram. The puffing plume P_0 continues to exist beyond its instability. We shall see as we analyze the various bifurcating states shown in Fig. 5 that P_0 continues to influence the dynamics, acting as a pacemaker with all bifurcating states inheriting the puffing frequency ω_0, with $\omega_0 \approx 1.48 R_N$ over the range of Ra shown in the figure.

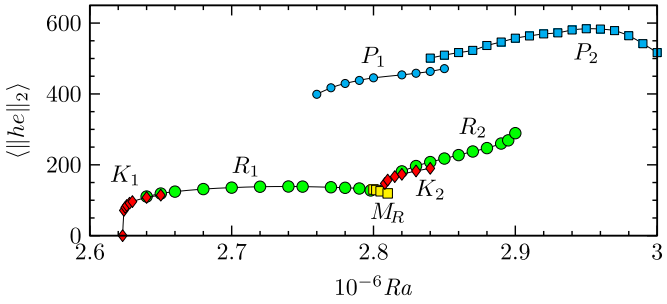

FIG. 5. Bifurcation diagram in terms of the time-averaged L_2 norm of the helicity density, $\langle \|\mathrm{he}\|_2 \rangle$, which is zero for the puffing plume P_0. The dynamics associated with the bifurcating quasiperiodic plume states K_1, K_2, R_1, and R_2 and the more complicated spatiotemporal plumes M_R, P_1, and P_2 are described in the text.

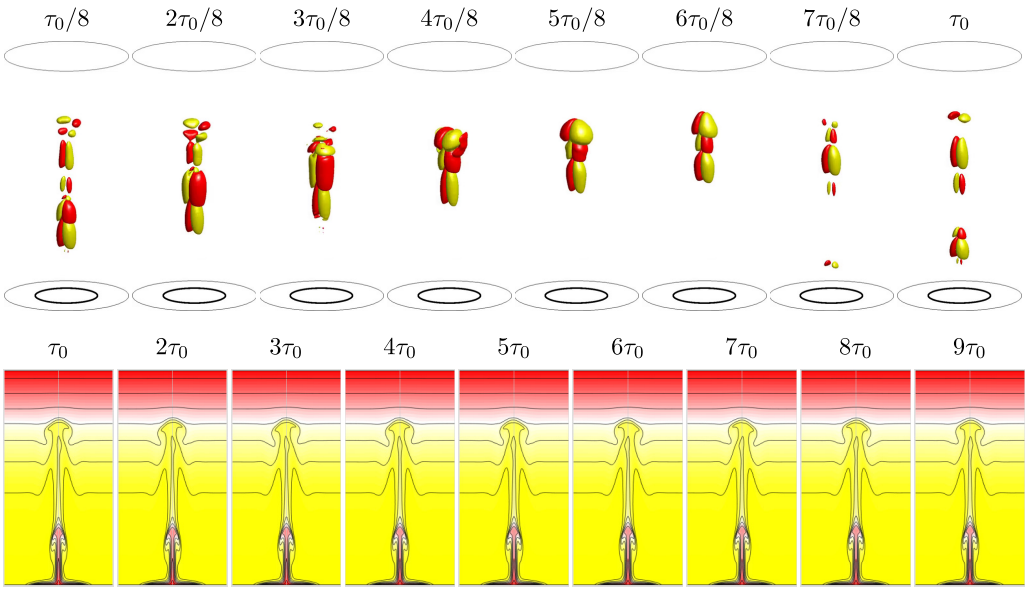

FIG. 6. Bifurcated quasiperiodic state K_1 at $\mathrm{Ra} = 2.64 \times 10^6$. The first row shows snapshots of helicity density isosurfaces at levels $\mathrm{he} = \pm 10^5$ equispaced in time over a puffing period τ_0; the gray circles at the top and bottom are drawn at the half radius of the cylinder. See movie 1 in the Supplemental Material [37] for an animation of this state over approximately nine puffing periods. The second row shows temperature contours in the central half of the meridional plane corresponding to the $\mathcal{K}$ reflection symmetry, strobed every puffing period, covering a little over one period of ω_1.

A. The K_1 wobbling puffing plume

The state bifurcating from P_0 is quasiperiodic, with two frequencies, the puffing frequency $\omega_0 \approx 1.48 R_N$ and a new frequency $\omega_1 \approx 0.170 R_N$, acquired at the Neimark–Sacker bifurcation. They are incommensurate, with a ratio $\omega_0/\omega_1 \approx 8.68$. With increasing Ra, this ratio varies only very slightly. In general, with parameter variations Neimark–Sacker bifurcations may lead to synchronization, where the frequency of the unstable limit cycle and the new frequency introduced at the bifurcation become a rational ratio p/q over an interval of the parameter (for example, Ra in our case). These synchronisation (resonance) tongues are only dynamically important when the integers p and q are smaller than 5, leading to the so-called strong resonances [38] which have been found to be relevant in some fluid dynamics problems [39]. When p and q are large, the synchronisation tongues are very narrow and the synchronized flows are almost indistinguishable from quasiperiodic solutions. In the range of parameters in our study, no synchronisation tongues with small p and q were found.

The structure of the helicity density of the bifurcated quasiperiodic plume is shown in the first row of Fig. 6, which depicts eight snapshots of the helicity density isosurfaces at $\mathrm{Ra} = 2.64 \times 10^6$, equispaced over a puffing period τ_0. Supplemental movie 1 [37] animates this state over approximately nine puffing periods. The solution clearly has a meridional symmetry plane, therefore the $\mathcal{K}$ reflection Z_2-symmetry is preserved whilst the $\mathcal{R}$ rotation $SO(2)$-symmetry is broken. We shall call these $\mathcal{K}$-invariant quasiperiodic states K_1 plumes. A flow which is $\mathcal{K}_\beta$ reflection symmetric about a meridional plane $\theta = \beta$ satisfies

$$[u, v, w, T](r, \theta, z, t) = \mathcal{K}_\beta [u, v, w, T](r, \theta, z, t) = [u, -v, w, T](r, 2\beta - \theta, z, t). \tag{15}$$

Consequently, K_1 plumes have zero helicity, $\mathrm{He} = 0$, while their helicity density is nonzero, $\mathrm{he} \neq 0$.

The K_1 solution branch actually consists of a whole circle of solutions, distinguished by the angle of the meridional symmetry plane β; any of the K_1 states can be obtained from another by applying

the rotation $\mathcal{R}_\alpha$ with an appropriate choice of α. The helicity density of a K_1 plume consists of two vertically oriented regions with opposite signs of helicity density either side of the reflection plane. These change sign and intensity as they rise along the plume with the puff. The puff wobbles in the reflection plane as it overshoots the neutral buoyancy level, as is evident in the second row of Fig. 6 showing isotherms in the meridional plane $\theta = \beta$, corresponding to the plume's $\mathcal{K}_\beta$ symmetry plane. These isotherms are snapshots that have been strobed once every puffing period τ_0, covering slightly more than one period τ_1 (the ratio of the frequencies is close to nine, $\omega_0/\omega_1 \approx 8.68$). These strobes show that as the plume overshoots the neutral buoyancy level, its tip undergoes lateral oscillations about the symmetry plane, while the bottom part of the plume shows very little variation, indicating that the flow in the bottom half is essentially τ_0-periodic (see movie 1 [37]). The amplitude of the oscillations is small as the K_1 plume considered is very near the bifurcation point. The behavior is reminiscent of the meandering observed in studies of other thermal plumes that preserve the $\mathcal{K}$-reflection symmetry [22,32].

B. The R_1 rotating puffing plume

The wobble in the K_1 plume increases with Ra, and very shortly after onset at $\mathrm{Ra} \approx 2.62 \times 10^6$, K_1 becomes unstable at $\mathrm{Ra} \approx 2.65 \times 10^6$. The $\mathcal{K}$ symmetry is broken at this bifurcation. The breaking of the reflection symmetry results in flows with nonzero He, and swirl is spontaneously generated. It is straightforward to enforce the $\mathcal{K}_0$ symmetry numerically, and we have continued the unstable K_1 plumes out to $\mathrm{Ra} \approx 2.78 \times 10^6$ (details are provided in Sec. V C).

A quantitative measure of the extent to which the $\mathcal{K}$ symmetry is broken is

$$S = \min_\beta \frac{\|\mathcal{K}_\beta \boldsymbol{u} - \boldsymbol{u}\|_2}{\|\boldsymbol{u}\|_2}. \tag{16}$$

The angle β is the angle which results in the smallest value of S, and is used to define the meridional plane that best approximates a reflection plane. This meridional plane will be called the S plane. If $\boldsymbol{u}$ is reflection-symmetric about the S plane $\theta = \beta$, then $\mathcal{K}_\beta \boldsymbol{u} = \boldsymbol{u}$ and $S = 0$. For small S, $\mathcal{K}_\beta \boldsymbol{u} \approx \boldsymbol{u}$. Since $\mathcal{K}_\beta$ is an isometry (i.e., it preserves norms) we have that $\|\mathcal{K}_\beta \boldsymbol{u}\|_2 = \|\boldsymbol{u}\|_2$, and $0 \leqslant S \leqslant 2$.

When K_1 loses stability at $\mathrm{Ra} \approx 2.65 \times 10^6$, the flow evolves to a new state R_1 with broken $\mathcal{K}$ symmetry. R_1 remains stable up to $\mathrm{Ra} \approx 2.8 \times 10^6$ and down to $\mathrm{Ra} \approx 2.64 \times 10^6$, so there is a small region of hysteresis in Ra where both K_1 and R_1 are stable. R_1 is also quasiperiodic, and its two fundamental frequencies are also denoted ω_0 and ω_1. The values of these two frequencies for the two states are virtually indistinguishable numerically. For both K_1 and R_1, ω_0 is the underlying puffing frequency, but ω_1 has very different dynamics associated with it for the two states. For K_1 this frequency is the slow wobble of the puff in the S plane, whereas the R_1 plume spontaneously attains swirl and this frequency is associated with the rotation.

At $\mathrm{Ra} = 2.70 \times 10^6$, roughly in the middle of the R_1 branch, the R_1 plume has the structure depicted in Fig. 7, covering a puffing period with nine equispaced in time snapshots of helicity density isosurfaces. Axial vorticity (associated with the swirl) is concentrated in the region where the puffs collide with the neutral buoyancy level, while the azimuthal vorticity is strongest in the rising plume near the hot spot on the bottom endwall, as in the basic state. Helicity density is evenly distributed along the plume, and shows a spiralling helical structure with azimuthal wave number $m = 1$. The flow structure at times 0 and τ_0 (separated by a puffing period) are identical, differing only in a finite rotation around the cylinder axis. Supplemental movie 2 [37] animates the flow over approximately 16 puffing periods. The movie also includes a view of the plume from above, showing how the S plane (indicated by a black line) rotates nonuniformly.

Figure 8 shows time series of β, the angle of the S plane, the meridional plane producing the best approximation to a $\mathcal{K}$-reflection symmetry plane, along with time series of the symmetry parameter S and of the helicity He, for R_1 at $\mathrm{Ra} = 2.70 \times 10^6$. The S plane rotates nonuniformly in the negative azimuthal direction, with a mean angular velocity around the cylinder axis given by the slope of the fitted regression line drawn in red in Fig. 8(c). This mean rotation is -0.1667, which is almost identical to $-\omega_1/R_N = -0.16674$. The rotation is not uniform, as is evident from the

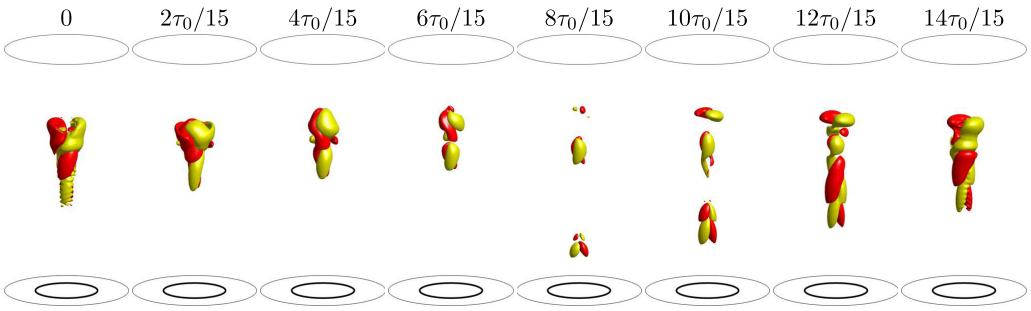

FIG. 7. Snapshots of the helicity density of R_1 at Ra $= 2.70 \times 10^6$ over approximately one puffing period $\tau_0 = 2\pi/\omega_0 = 1.382 \times 10^{-3}$. The isolevels are he $= \pm 2 \times 10^5$; the gray circles at the top and bottom are drawn at the half radius of the cylinder. Supplemental movie 2 [37] animates the flow over approximately 16 puffing periods.

figure and movie 2 [37]; there are periodic pulses during which the rotation reverses sign slightly for a short time. These pulses occur periodically with period $2\pi/\omega_0 \approx 4.25R_N$, corresponding to the underlying puffing period τ_0. The helicity, He, oscillates about a mean $\langle \mathrm{He} \rangle \approx -14.0$, corresponding to the mean retrograde rotation of the plume. The helicity is slightly positive during a part of the puffing period, corresponding to the times during which the rising puff and the receding prior puff collide near the neutral buoyancy level. At other times, associated with the formation and rise of the puff from the hot spot, He is strongly negative and the symmetry measure S is largest, suggesting that swirl is generated near the hot spot when a new puff is formed and starts to rise.

As the mean helicity, $\langle \mathrm{He} \rangle$, of the R_1 plume is nonzero, the reflected plume (its $\mathcal{K}$ conjugate) rotates about the axis in the opposite direction, so there are two branches of quasiperiodic R_1 plumes that are symmetry related by a $\mathcal{K}$ reflection. R_1 is a quasiperiodic solution, and when its two frequencies are incommensurate (as is the case), it densely fills a two-torus. Applying the rotation symmetry $\mathcal{R}_\alpha$ to R_1 results in a *different solution*, but it also lies on the *same torus*. So, the torus *as a set* is $\mathcal{R}_\alpha$-invariant, and the torus is the union of all the individual solutions of type R_1 obtained by applying $\mathcal{R}_\alpha$. An individual R_1 is not $\mathcal{R}_\alpha$-invariant (it is not pointwise invariant), but lives on an $\mathcal{R}$-invariant two-dimensional torus (which is setwise invariant). For more details see Marques and Lopez [40] and Lopez and Marques [41]. The R_1 plumes have rising puffs that are not axisymmetric

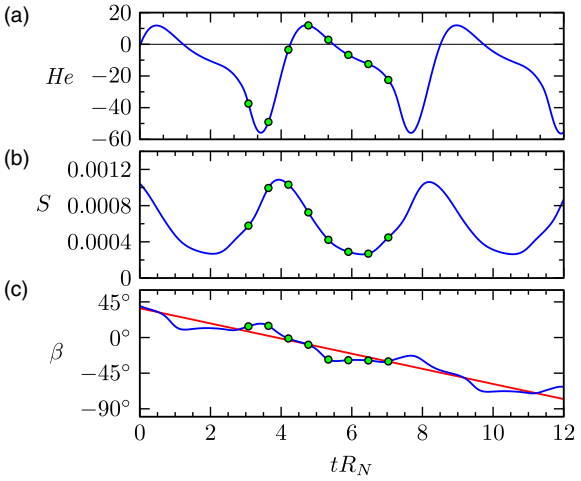

FIG. 8. Time series of (a) the helicity He, (b) the symmetry parameter S, and (c) the S-plane angle β, for R_1 at Ra $= 2.70 \times 10^4$. The symbols correspond to the 16 snapshots shown in Fig. 7.

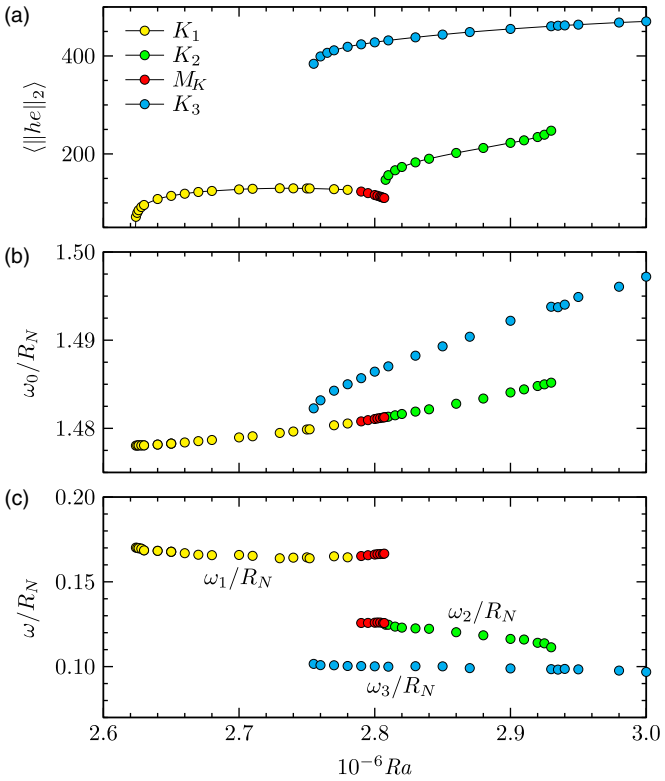

FIG. 9. (a) Bifurcation diagram restricted to the $\mathcal{K}_0$-invariant subspace, and (b, c) frequencies of the $\mathcal{K}_0$ subspace restricted plumes.

and are rotating (i.e., spiralling); the one depicted in Fig. 7 has a left-handed orientation, and the $\mathcal{K}$-conjugate plume has a right-handed orientation.

What makes the bifurcation sequence involving P_0, K_1, and R_1 interesting is the presence of the $O(2)$ symmetry. In Appendix B, we briefly describe the dynamical systems theory of a Hopf bifurcation from a steady state breaking $O(2)$ symmetry. Those results also apply to Neimark–Sacker bifurcations from a periodic solution breaking $O(2)$ symmetry [42]. These considerations are useful in unraveling the interconnections between the axisymmetric puffing plume P_0, the two $\mathcal{K}$-conjugate swirling R_1 plumes, and the circle of $\mathcal{K}$-invariant wobbling K_1 plumes.

C. Plumes in the $\mathcal{K}$-invariant subspace

At $\mathrm{Ra} \approx 2.805 \times 10^6$, the R_1 plume suddenly loses stability. The K_1 plume however, is already unstable for $\mathrm{Ra} \gtrsim 2.65 \times 10^6$, but by restricting the simulations to the $\mathcal{K}$-invariant subspace, it is stable in that subspace out to $\mathrm{Ra} \approx 2.78 \times 10^6$. In this subsection, we explore the dynamics in the $\mathcal{K}_0$ subspace, in which the S reflection plane is fixed at $\theta = 0^\circ$. Figure 9 is the bifurcation diagram in this subspace, and should be compared to the bifurcation diagram in the full space shown in Fig. 5.

For $2.81 \times 10^6 \lesssim \mathrm{Ra} \lesssim 2.94 \times 10^6$, simulations in the $\mathcal{K}_0$ subspace with a broad range of initial conditions settle onto a plume state that is very similar to K_1, which we simply call K_2. It is also quasiperiodic, with one frequency corresponding to the puffing frequency $\omega_0 \approx 1.48 R_N$. Figure 9(b) is a plot of ω_0/R_N for K_1 and K_2, showing that ω_0/R_N is continuous across the two plumes and varies very slowly with Ra; this is simply the frequency of the axisymmetric puffing plume P_0. The other frequency in K_2 is ω_2, associated with the wobbling in the symmetry plane $\theta = 0^\circ$. The wobbles in

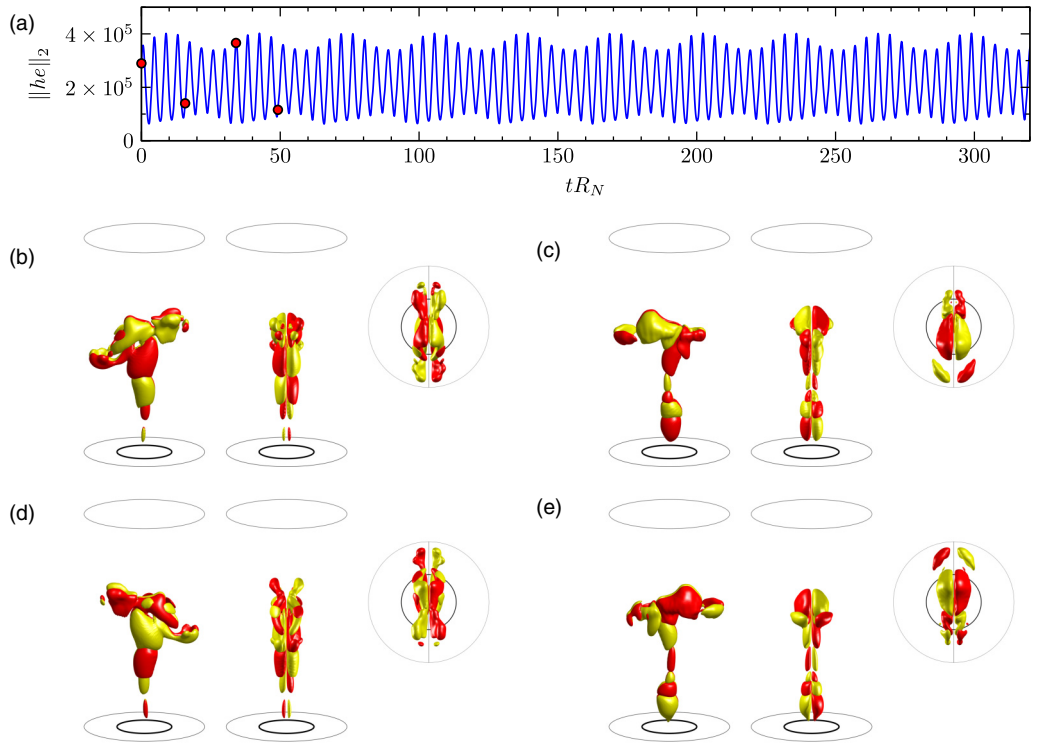

FIG. 10. (a) Time series of the L_2 norm of the helicity, $\|\mathrm{he}\|_2$, for K_3 at $\mathrm{Ra} = 2.95 \times 10^6$. The four red symbols indicate the times corresponding to the snapshots of the helicity density isosurfaces in panels (b–e), shown from two perspectives rotated by 90° and a top view. The isolevels are $\mathrm{he} = \pm 4 \times 10^5$; the gray circles at the top and bottom are drawn at the half radius of the cylinder. Supplemental movie 3 [37] shows an animation over the time in panel (a).

K_2 are of the same type as in K_1 described earlier, but with a slightly lower frequency; see Fig. 9(c). For a small interval in Ra, near $\mathrm{Ra} \approx 2.80 \times 10^6$, there is a plume with three incommensurate frequencies, consisting of ω_0, ω_1 and ω_2; this is a mixed mode of K_1 and K_2 and we refer to it as M_K. It is also a puffing plume with a wobble in its symmetry plane, but now the frequency of the wobble is slowly modulated with the beat frequency corresponding to the difference $|\omega_1 - \omega_2| \approx 0.04 R_N$.

For $\mathrm{Ra} \gtrsim 2.94 \times 10^6$, K_2 is no longer stable and the flow evolves to yet another plume with a wobble in the symmetry plane, called K_3. This plume extends to larger Ra (we only report up to $\mathrm{Ra} = 3 \times 10^6$ here), and down to $\mathrm{Ra} \approx 2.75 \times 10^6$, so that it coexists with K_1, K_2, and M_K. The K_3 plumes have a slightly (approximately 1%) higher ω_0 and their second frequency $\omega_3 \approx 0.1 R_N$ is smaller than those of K_1 and K_2 (see Fig. 9). A time series of the L_2 norm of the helicity density, $\|\mathrm{he}\|_2$, for K_3 at $\mathrm{Ra} = 2.95 \times 10^6$ is shown in Fig. 10(a). The time series shows oscillations at the puffing frequency ω_0 that are modulated. From Fig. 9, $\omega_0/\omega_3 \approx 14.9$ but the modulation frequency in the time series is $0.5\,\omega_3$. This is due to $\|\mathrm{he}\|_2$ being a squared quantity. The snapshots of he isosurfaces shown in Figs. 10(b)–10(e) are equispaced over one half modulation period, covering approximately 8 puffing periods. They show a large anvil-like structure near the neutral buoyancy level that is aligned with the symmetry plane; the anvil tilts one way over these 8 puffing periods, and then tilts back over the next 8 puffing periods. Supplemental movie 3 [37] shows an animation over approximately 80 puffing periods [the length of the time series in Fig. 10(a)]. As ω_0 and ω_3 are not commensurate, the plume never repeats its structure, but the combined effects of the puffing and the anvil tilting are well illustrated.

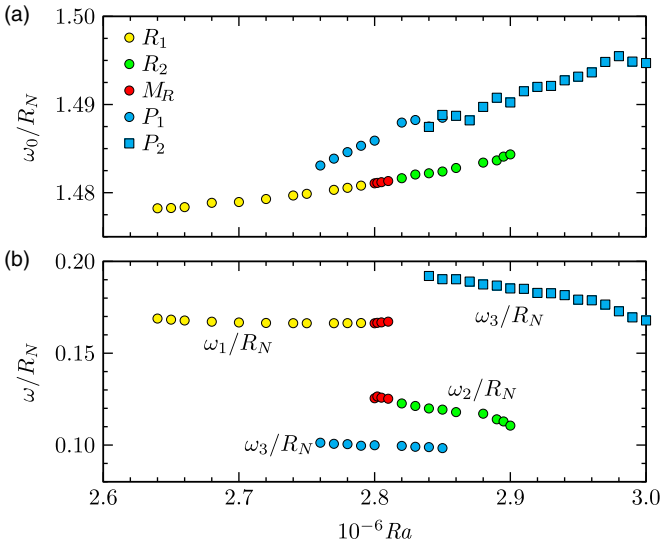

FIG. 11. Frequencies of R_1, R_2, M_R, P_1, and P_2.

D. The R_2 rotating puffing plume

Returning to the full space, the dynamics is considerably more complicated. The K_1, K_2, and K_3 plumes at a given point in parameter space consist of whole circles of such plumes, parameterized by the orientation of their symmetry plane $\theta = \beta$. The restriction to the $\mathcal{K}_0$ symmetry subspace considered above selected exactly one plume with $\beta = 0^\circ$. In the full space, K_1 is unstable for $\mathrm{Ra} \gtrsim 2.65 \times 10^6$, K_2 is stable from its emergence at $\mathrm{Ra} \approx 2.81 \times 10^6$ and loses stability at $\mathrm{Ra} \approx 2.84 \times 10^6$, and the whole of the K_3 branch is unstable. With the K-plumes being unstable in the full space over a considerable range of Ra, in this subsection we explore what states are stable in this range of Ra.

As noted earlier, the R_1 plume is stable for $2.64 \times 10^6 \lesssim \mathrm{Ra} \lesssim 2.805 \times 10^6$. For $2.82 \times 10^6 \lesssim \mathrm{Ra} \lesssim 2.90 \times 10^6$ there is another branch of rotating puffing plumes, which we call R_2. These have the same dynamics as R_1, but their frequency ω_2 is lower; see Fig. 11.

At $\mathrm{Ra} = 2.85 \times 10^6$, roughly in the middle of the R_2 branch, the R_2 plume has the structure depicted in Fig. 12, showing six snapshots of the helicity density isosurfaces over one puffing period. The helicity density is evenly distributed along the plume, and shows a spiralling helical structure with azimuthal wave number $m = 1$. The R_2 plume is similar to the R_1 plume, but more intense (larger $\|\mathrm{he}\|_2$). However, the puff that emerges periodically from the hot spot is spiralling, whereas for R_1 it is not spiralling and has an approximate $\mathcal{K}$ symmetry (see Fig. 7). At times separated by a puffing period, the R_2 structure is identical, but rotated about the cylinder axis. Figure 13 shows time series of He, S, and β for R_2 at $\mathrm{Ra} = 2.85 \times 10^6$. The S plane rotates nonuniformly in the negative azimuthal direction, with a mean angular velocity around the cylinder axis given by the slope of the fitted regression line drawn in red in Fig. 13(c). This mean rotation is -0.1207, which is very close to $-\omega_2/R_N = -0.1193$. Supplemental movie 4 [37] animates the flow over approximately 12 puffing periods, showing two perspective views of helicity density isosurfaces. The view from the top includes a line traversing the axis showing the orientation of the S plane, illustrating the modulated rotation of the plume. The helicity He oscillates about a mean value $\langle \mathrm{He} \rangle \approx -154.7$, corresponding to the retrograde rotation of the plume. The helicity is slightly positive and S is maximal during a part of the puffing period when the rising puff collides with the prior receding puff, as was the case for the R_1 plumes. Overall, S is larger (by approximately a factor of 5) for R_2 compared to R_1; this is a consequence of the swirl in the R_2 puff as it emerges from the hot spot.

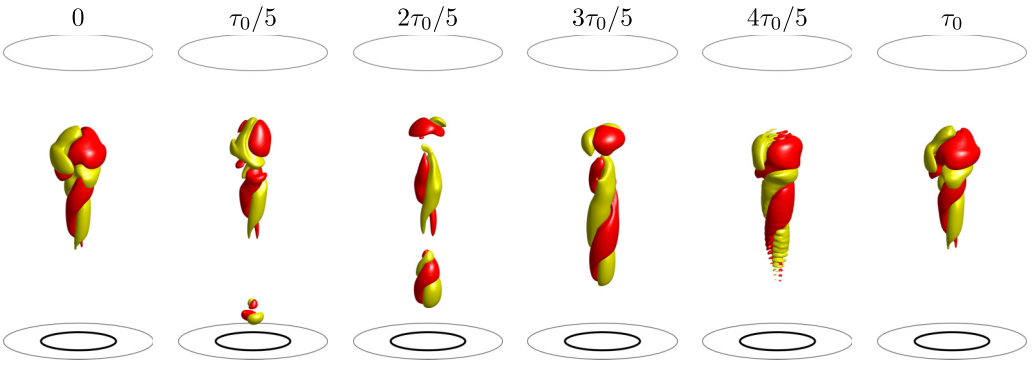

FIG. 12. Snapshots of the helicity density of R_2 at Ra $= 2.85 \times 10^6$ over approximately one puffing period. The isolevels are he $= \pm 2 \times 10^5$; the gray circles at the top and bottom are drawn at the half radius of the cylinder. Supplemental movie 4 [37] animates the flow over approximately 12 puffing periods.

In between the R_1 and R_2 branches, for $2.805 \times 10^6 \lesssim \text{Ra} \lesssim 2.81 \times 10^6$, there is a mixed mode of R_1 and R_2, called M_R, but it is more complicated than the mixed mode M_K described earlier in the $\mathcal{K}_0$ subspace. The added complication stems from the fact that R_1 and R_2 each have two parities as a result of the broken $\mathcal{K}$ symmetry; each pair consists of a plume that rotates in the positive and another rotating in the negative azimuthal direction. Which parity is realized depends on initial conditions. The mixed mode M_R is hence a mixed mode between R_1, $\mathcal{K}R_1$, R_2, and $\mathcal{K}R_2$, and the resulting plume has frequencies ω_0 (from the underlying puffing), $\pm\omega_1$, and $\pm\omega_2$ (the signs $\pm$ signify rotation in the positive and negative azimuthal directions). Figures 14(a) and 14(b) show time series of he and S for a M_R plume at Ra $= 2.805 \times 10^6$. Clearly evident is a low-frequency beating corresponding to $\omega_1 - \omega_2$. Figure 14(c) shows the time series of β, the S-plane angle. This angle varies irregularly in time; there are relatively long stretches of time (several puffing periods) during which the mean rotation is in one sense, with sudden switches to the other sense of rotation. During these intervals, the mean slopes of $\partial\beta/\partial t$ are approximately $\pm\omega_1/R_N$ and $\pm\omega_2/R_N$.

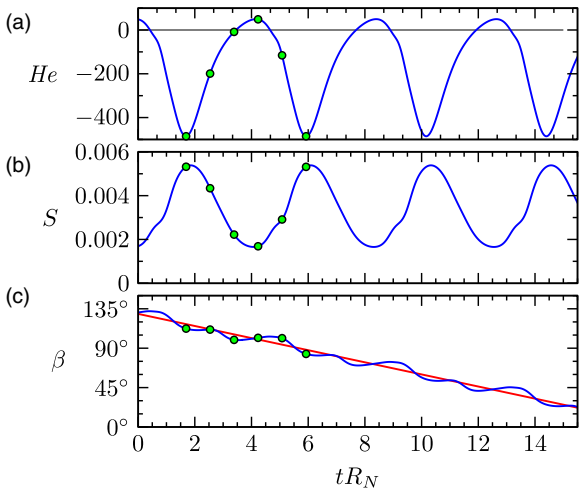

FIG. 13. Time series of (a) the helicity He, (b) the symmetry parameter S, and (c) the S-plane angle β, of R_2 at Ra $= 2.85 \times 10^6$. The symbols correspond to the 6 snapshots shown in Fig. 12.

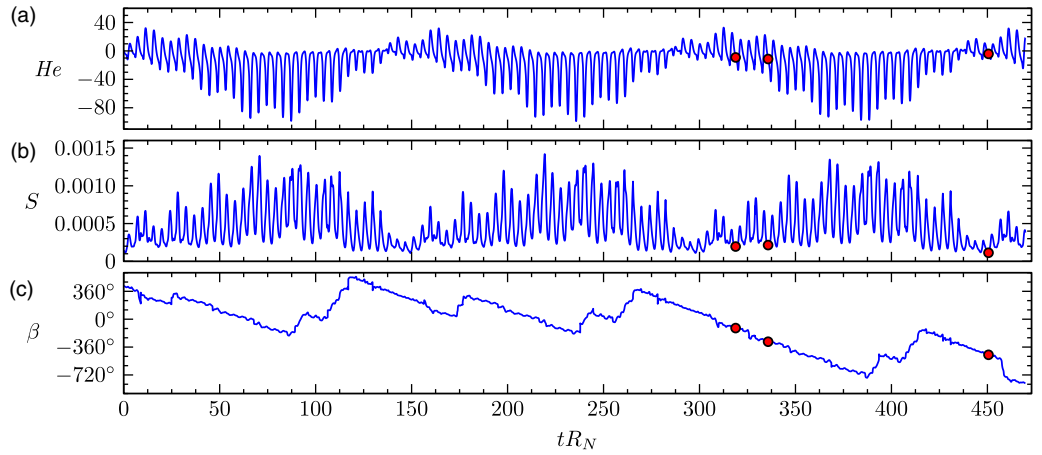

FIG. 14. Time series of (a) the helicity He, (b) the symmetry parameter S, and (c) the S-plane angle β, for the mixed mode M_R at Ra $= 2.805 \times 10^6$. The three red points correspond to the snapshots shown in Fig. 15.

The reversals in the mean sense of rotation are not correlated with the beat frequency. Supplemental movie 5 [37] animates the mixed mode M_R at Ra $= 2.805 \times 10^6$ over the time interval $313.3 \leqslant tR_N \leqslant 469.9$, corresponding to approximately one beat period, illustrating the complex dynamics. In the movie, the helicity density isosurfaces are shown from two perspective views. In the view from the top, the S plane is indicated by a line drawn through the axis; its irregular orientation as reported from the time series is well illustrated. Three snapshots from the movie are shown in Fig. 15, corresponding to the times indicated by red symbols in the time series in Fig. 14. The first of these snapshots shows a phase where M_R resembles R_1, with the plume structure as it

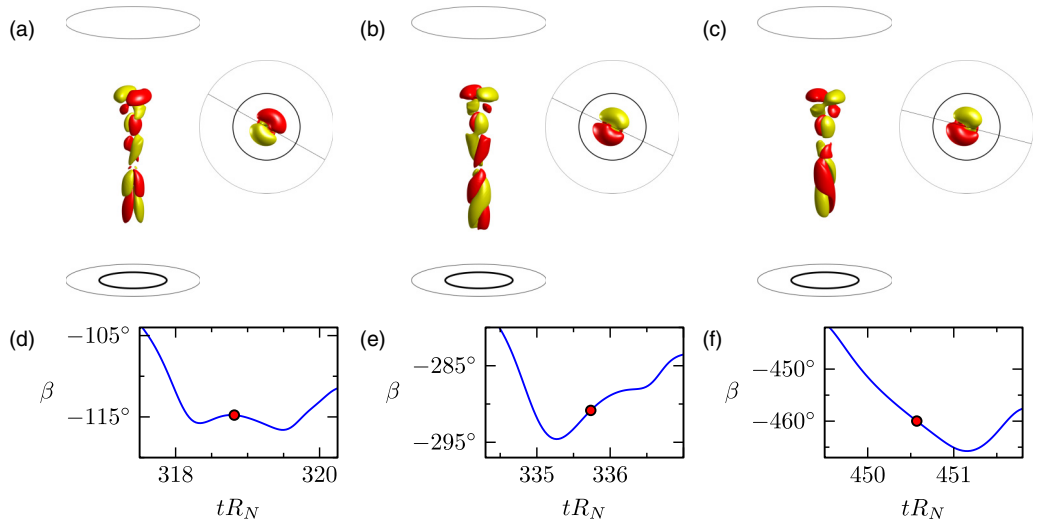

FIG. 15. Snapshots of helicity density isosurfaces, he $= \pm 10^5$, of the mixed mode M_R at Ra $= 2.805 \times 10^6$, at times (a) $tR_N = 318.812$, (b) $tR_N = 335.732$, and (c) $tR_N = 450.567$, corresponding to the red symbols in the time series in Fig. 14; the gray circles at the top and bottom are drawn at the half radius of the cylinder, and (d, e, f) show closeups of the time series of β in the neighbourhoods of these times. Supplemental movie 5 [37] animates this case over the time interval $tR_N \in (313.3, 469.9)$.

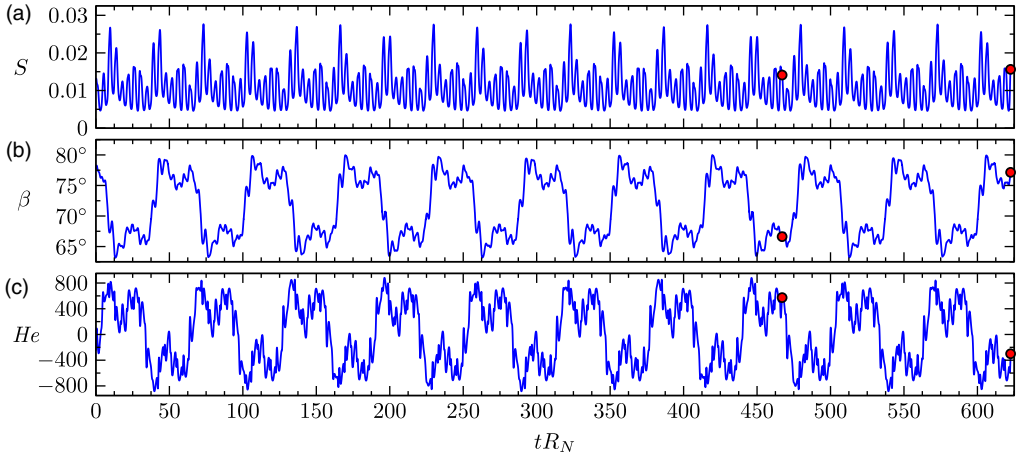

FIG. 16. Time series of (a) the symmetry parameter S, (b) the S-plane angle β, and (c) helicity He of P_1 at $\mathrm{Ra} = 2.77 \times 10^6$. The two red points correspond to the snapshots shown in Fig. 17.

leaves the hot spot having a well-defined S plane and $\partial\beta/\partial t \approx 0$, whereas the other two snapshots show phases where M_R resembles R_2 with the plume structure as it leaves the hot spot having a positive spiral and $\partial\beta/\partial t > 0$ in one and a negative spiral and $\partial\beta/\partial t < 0$ in the other.

E. Pulse-wave plumes P_1 and P_2

For $\mathrm{Ra} \gtrsim 2.9 \times 10^6$, all of the plumes described so far are unstable. Any initial condition for larger Ra evolves to one of the upper branch states labeled P_1 and P_2 in Figs. 5 and 11. Using that state as an initial condition for smaller and larger Ra, the solution branches P_1 and P_2 are mapped out. These are also quasiperiodic states with two incommensurate frequencies. As with the other unsteady plumes, one of the frequencies corresponds to the puffing frequency ω_0, although this is slightly larger than that in the rotating plumes R_1 and R_2, which are stable and coexist with P_1 and P_2 for a range of Ra, as shown in Fig. 9. Figure 17 shows a pair of snapshots of helicity density for a P_1 plume at $\mathrm{Ra} = 2.77 \times 10^6$. It has many features in common with the K_3 plume (compare with Fig. 10), in particular the large anvil at the neutral buoyancy level. P_1 also has an approximate $\mathcal{K}$ symmetry, most obvious in the lower part of the plume as it rises from the hot spot, and the symmetry

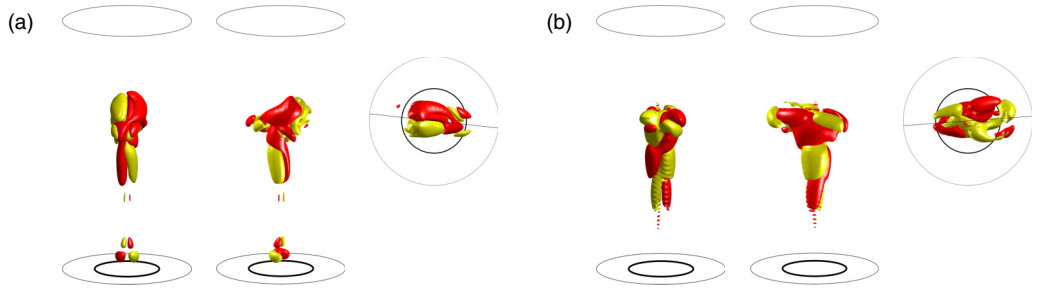

FIG. 17. Snapshots of helicity density isosurfaces, $\mathrm{he} = \pm 4.5 \times 10^5$, of P_1 at $\mathrm{Ra} = 2.77 \times 10^6$, shown from two perspectives rotated by 90° and a top view, at two times: (a) $tR_N = 467$ during which $\mathrm{He} < 0$ and (b) $tR_N = 622.6$ with $\mathrm{He} > 0$; the gray circles at the top and bottom are drawn at the half radius of the cylinder. Supplemental movie 6 [37] animates this case over the extent $tR_N \in (467, 622.9)$ of the time series shown in Fig. 16.

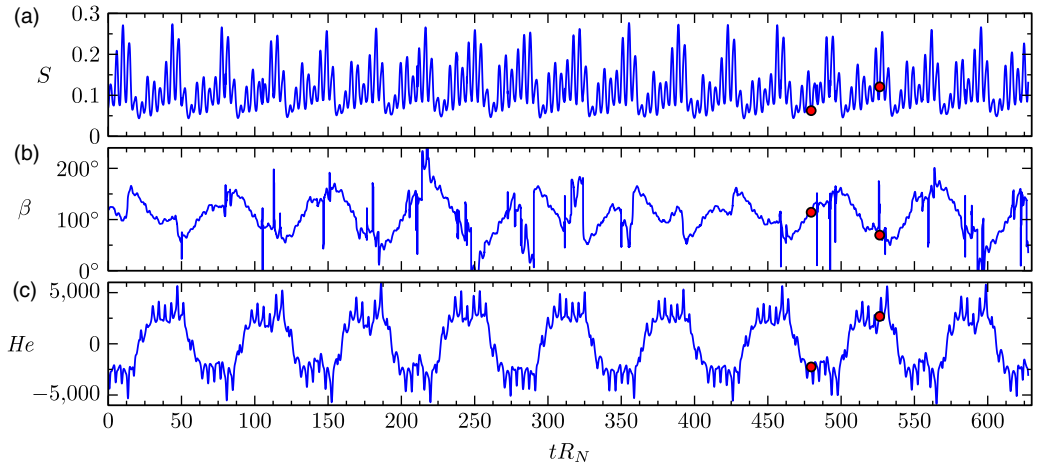

FIG. 18. Time series of (a) the symmetry parameter S, (b) the S-plane angle β, and (c) helicity He of the pulse-wave P_2 at $\mathrm{Ra} = 2.93 \times 10^6$. The two red points correspond to the snapshots shown in Fig. 19.

is broken most strongly as it approaches the neutral buoyancy level and in the anvil region. However, P_1 does not have an S plane at a fixed azimuthal angle and its helicity He is nonzero. Figure 16 shows time series of the symmetry measure S, the angle of the S plane β, and the helicity He. These are strongly modulated. These time series are quite informative; S spikes every puffing period as the puff reaches the neutral buoyancy level, and there is a larger spike (or two) approximately every 6 or 7 puffing periods. These larger spikes in S are associated with a reorientation of the S plane between $\beta \approx 66.62^\circ$ and 76.66°. During the time intervals with $\beta \approx 66.62^\circ$, the helicity is positive and during the intervals with $\beta \approx 76.66^\circ$ it is negative. This modulation period defines ω_3, which is shown in Fig. 11(b). It is virtually the same as ω_3 for the K_3 plumes shown in Fig. 9(c). However, for K_3 plumes ω_3 is associated with the wobbling of the anvil in the S plane, which remain at a fixed angle, whereas for the P_1 plumes ω_3 is associated with the S planes pulsing between different angles β. Supplemental movie 6 [37] animates the helicity density over a time interval in tR_N of 150, which covers approximately five of these pulses.

Although the P_2 plumes have very similar time series of S, β, and He as the P_1 plumes (compare Figs. 16 and 18) they have very different spatiotemporal characteristics. Figure 19 shows a pair of

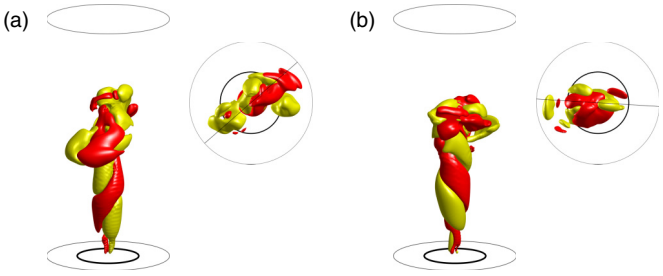

FIG. 19. Snapshots of helicity density isosurfaces, $\mathrm{he} = \pm 3.0 \times 10^5$, of P_2 at $\mathrm{Ra} = 2.93 \times 10^6$, shown from one perspective and a top view, at two times: (a) $tR_N = 479.55$ during which $\mathrm{He} < 0$ and (b) $tR_N = 526.31$ with $\mathrm{He} > 0$; the gray circles at the top and bottom are drawn at the half radius of the cylinder. Supplemental movie 7 [37] animates this plume over the extent $tR_N \in (462, 628)$ of the time series shown in Fig. 18.

snapshots of the helicity density of P_2 at $\mathrm{Ra} = 2.93 \times 10^6$ approximately one pulse period apart. The most striking difference with P_1 (Fig. 17) is that the plume is twisted as it leaves the hot spot, much like what is the case with the rotating puffing plumes (compare with R_2 in Fig. 12). As such, there is no approximate reflection plane and the symmetry parameter S is an order of magnitude larger than it is for P_1. Like with P_1, the time series of S for P_2 also shows spikes every puffing period, indicating that the plume breaks $\mathcal{K}$ symmetry more strongly as the puff reaches the neutral buoyancy level, as well as one or two much larger spikes every seven or eight puffs. During the seven or eight puffing periods between the larger spikes, the helicity is of one sign and then undergoes a pulse changing sign. Although the S plane is no longer meaningful in terms of an approximate $\mathcal{K}$ symmetry, the minimizing angle β is still illustrative. The angle β, on average, decreases whilst He is positive and increases whilst He is negative. Supplemental movie 7 [37] animates helicity density of this plume over a couple of these pulses reversals.

VI. CONCLUSIONS

The initial goal of the present study was to find an ambient stratification distribution in which a localized plume displays competition between puffing, wobbling, and swirling dynamics as the Rayleigh number, Ra, is increased. In a uniform ambient, the first bifucation with increasing Ra retains the spatial symmetries of the system [$O(2)$ symmetry—invariance to rotations and reflections about the plume axis], but introduces a temporal periodicity as a localized puff at the base of the plume periodically forms and then rises. With increasing Ra, the puff rises faster and its collision with the top leads to a myriad of symmetry-breaking instabilities and the dynamics become very complicated. For the most part, the symmetry-broken plume retains a meridional symmetry plane and the puffs wobble in this plane while they rise, and the complications come about as the wobbling puffs break up following their collisions with the top.

In a linearly stratified ambient, if the stratification is sufficiently strong, then vertical motions tend to be suppressed and so the plume tries to rise but is twisted; the strong stratification leads to a breaking of the rotation symmetry (invariance to rotations about the plume axis), at which point swirl is spontaneously generated. The periodic puffs appear as a secondary instability leading to a modulated swirling plume.

In the present problem, with a mixed ambient, the plume also undergoes symmetry breaking bifurcations that are a blend of those found in the other two scenarios. As in the uniform ambient case, the primary instability with increasing Ra is the axisymmetric puffing instability. The puffing mode persists throughout all the subsequent instabilities, acting as a pacemaker for the dynamics. Both the wobbling and swirling instability mechanisms come into play almost simultaneously with further increases in Ra, resulting in an interesting sequence of bifurcations involving mode competition and hysteresis. The first set of symmetry breaking dynamics can be well described using normal form theory for the breaking of $O(2)$ symmetry of equilibria applied to maps; this is due to the symmetric state being a limit cycle, the puffing plume. The plume states involved have relatively low intensity, quantified by their helicity. Over a considerable range of Ra, there coexists a disjoint set of more intense plume states with much larger helicity.

The more intense "upper branch" plume states also have dynamics associated with $O(2)$ symmetry breaking, such as pulse waves resulting from the breaking of $O(2)$ symmetry of steady state [43], but the normal form theory for these does not work as well. The normal form reduced system of equations has additional symmetries which result in heteroclinic cycles which are replaced by the pulse waves in the fully nonlinear setting. Nevertheless, the pulse plumes we have described have much in common with the pulse waves. These solutions manifest a variety of behaviors: the meridional symmetry plane of the wobbling plumes is partially broken, resulting in an approximate S plane whose meridional orientation either oscillates about some fixed azimuthal angle, pulses between two distinct azimuthal angles, or quasiuniformly drifts in azimuth indicating a clear signal of the influence of the spontaneous generation of swirl. These behaviors alternate with varying degrees of relative dominance as Ra is increased, resulting in many of the complex solutions found.

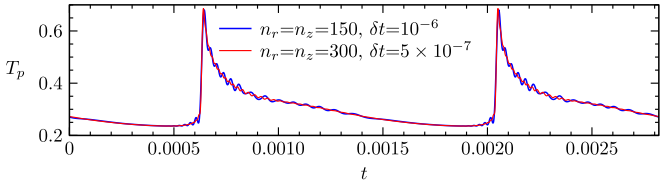

FIG. 20. Time series of the temperature at the center of the cylindrical domain, T_p, for P_0 at Ra $= 2.6 \times 10^4$, computed with the spatial and temporal resolutions as indicated.

ACKNOWLEDGMENT

This work was supported by the Spanish Ministerio de Ciencia e Innovación Grant No. PID2020-114043GB-100.

The authors report no conflict of interest.

APPENDIX A: RESOLUTION TEST

Here, we compare the axisymmetric puffing plume P_0 at Ra $= 2.6 \times 10^4$ computed with the resolution used throughout the rest of the paper (Chebyshev polynomials of degrees 150 in both r and z, and time step $\delta t = 10^{-6}$) to that computed with twice the resolution (Chebyshev polynomials of degrees 300 in both r and z, and time step $\delta t = 5 \times 10^{-7}$).

Figure 20 shows the evolution over two puffing periods of the temperature at the center of the cylindrical domain using the two resolutions considered. The large spikes in the figure correspond to the arrival of the rising puff to the center of the domain; the time between these spikes (the puffing period) is unaffected by the resolution used, but the small ripples which are evident either side of the large spikes are diminished with the increased resolution. Figure 21 shows isotherms at two instants of the puffing period τ_0, corresponding to minimal and maximal ripples near the axis. At the resolution used throughout the paper ($n_r = n_z = 150$, $\delta t = 10^{-6}$), ripples are not present at times near $t = 0.00024$, while they are clearly noticeable at $t = 00092$. Supplementary movie 8 [37] animates this P_0 plume computed with the two resolution over one puffing period. The ripples are evidently due to the resolution used. Nevertheless, the solution at the lower resolution is in the asymptotically converged regime, and these small ripples do not affect the dynamics of the results. In particular, the puffing period, which is the pacesetter for all the dynamics reported, is unaffected by the change in resolution, nor is the overall structure of the plume. The marginality of the resolution is borne out in Fig. 22, which shows the L_2 norm of the spectral coefficients of

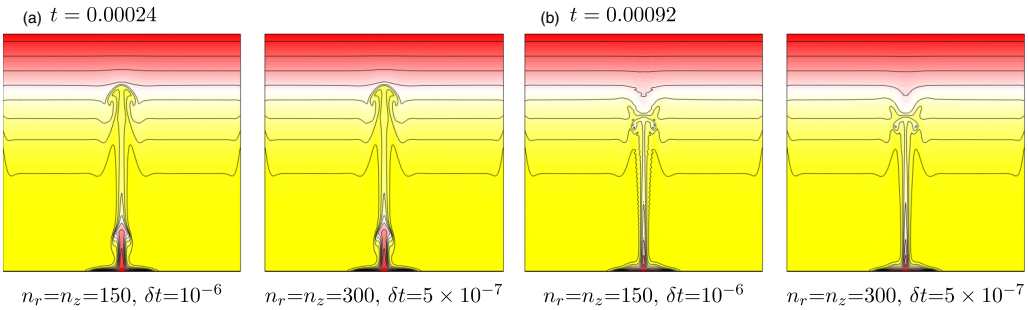

FIG. 21. Isotherms of P_0 at two different instants in a puffing period $\tau_0 \approx 0.00142$: (a) at $t = 0.00024 \approx 0.169\tau_0$ corresponds to minimal oscillations near the axis and (b) at $t = 0.00092 \approx 0.648\tau_0$ corresponds corresponds to maximal oscillations; isotherms are shown using the different resolutions as indicated. Supplementary movie 8 [37] animates the isotherms at both resolutions over one puffing period.

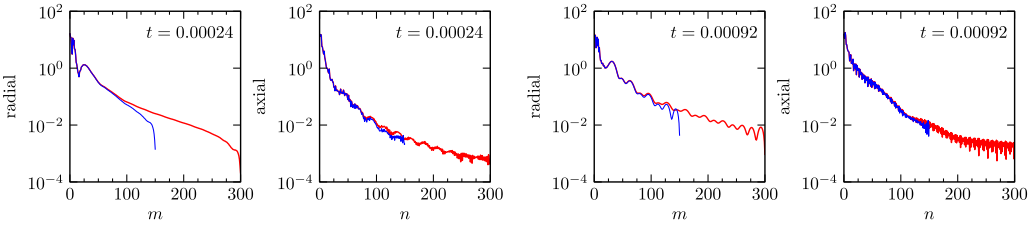

FIG. 22. Spectral convergence of P_0 at $\mathrm{Ra} = 2.6 \times 10^4$, at the two times used in Fig. 21.

the velocity modulus $|\boldsymbol{u}|$, in the radial and axial directions, for solutions with the two resolutions at the two times used in Fig. 21. The convergence is better when the ripples near the axis are absent ($t = 0.00024$). Nevertheless, at all times, and even with the lower resolution, the spectral coefficients decay by at least three orders of magnitude. As such, the results presented in the paper use the lower marginal resolution, which makes the study affordable; doubling the resolution increases the computation time by well over an order of magnitude. Whether the ripples are purely a numerical artifact is not completely clear, as there is a physical mechanism for their presence, and they have been observed in similar problems as reported by Vincent *et al.* [36]. However, the fact that the amplitude and period of the ripples are halved by doubling the resolution suggests a numerical origin of these oscillations.

APPENDIX B: BIFURCATIONS BREAKING $O(2)$ SYMMETRY: NORMAL FORMS

According to Crawford and Knobloch [15] and Knobloch [44], a Hopf bifurcation from a steady state that breaks $O(2) = SO(2) \rtimes Z_2$ symmetry can result in either standing or rotating waves. Due to the Z_2 reflection symmetry, there are two rotating waves with opposite sense of rotation. So, there are three different solutions that bifurcate simultaneously, and which one is observed depends on the specifics of the problem and the initial conditions. The normal form, at low order and assuming nondegeneracy conditions, is

$$\begin{aligned} \dot{r}_1 &= r_1\left(\mu - a r_1^2 - b r_2^2\right), \\ \dot{r}_2 &= r_2\left(\mu - a r_2^2 - b r_1^2\right), \\ \dot{\phi}_1 &= \dot{\phi}_2 = \omega, \end{aligned} \tag{B1}$$

where μ is the bifurcation parameter and $\mu = 0$ is its critical value for the bifurcation. The center manifold has codimension four, with complex amplitudes $r_1 e^{i\phi_1}$ and $r_2 e^{i\phi_2}$. The phase dynamics is trivial and decouples from the amplitude dynamics, which is two-dimensional. The nondegeneracy conditions are $a \neq 0$ and $a \pm b \neq 0$. The normal form has four fixed points,

$$\begin{aligned} Q_0 &: \quad (r_1, r_2) = (0, 0), \\ Q_1 &: \quad (r_1, r_2) = (\sqrt{\mu/a}, 0), \\ Q_2 &: \quad (r_1, r_2) = (0, \sqrt{\mu/a}), \\ Q_3 &: \quad (r_1, r_2) = [\sqrt{\mu/(a+b)}, \sqrt{\mu/(a+b)}]. \end{aligned} \tag{B2}$$

Strictly speaking, since the phases ϕ_1 and ϕ_2 have the same frequency ω, Q_1, Q_2, and Q_3 are periodic orbits, and Q_0 is a true fixed point. It is only in the restricted two-dimensional normal form for the amplitude equations of r_1 and r_2 that they are all fixed points. If the bifurcation is supercritical, so that the three periodic solutions Q_1, Q_2, and Q_3 exist for $\mu > 0$, then $a > 0$ and $a + b > 0$.

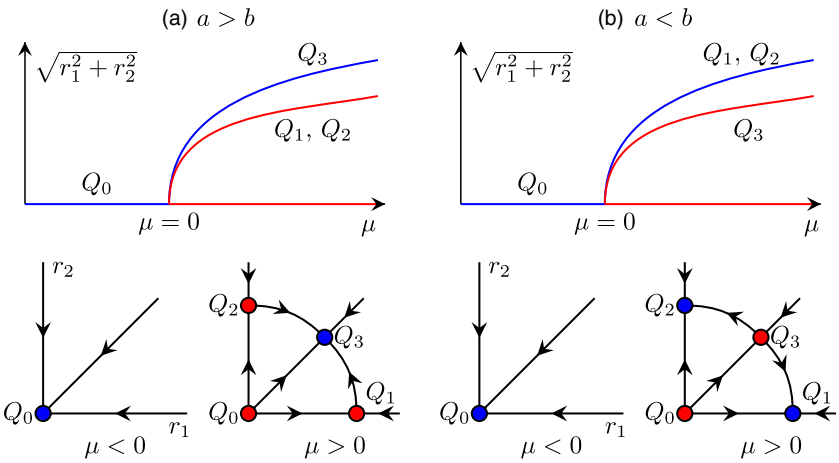

FIG. 23. Bifurcation diagrams of the supercritical Hopf bifurcation breaking $O(2)$ symmetry associated with the normal form (B1) for cases (a) $a > b$ and (b) $a < b$, and the corresponding phase portraits. The blue (red) curves and symbols represent stable (unstable) solutions.

The actions of the rotation symmetry $\mathcal{R}_\alpha$, that generates the $SO(2)$ group, and the reflection symmetry $\mathcal{K}_\beta$, that generates the Z_2 group, on the normal form are

$$\begin{aligned} \mathcal{R}_\alpha &: [r_1, r_2, \phi_1, \phi_2] \mapsto [r_1, r_2, \phi_1 + m\alpha, \phi_2 - m\alpha], \\ \mathcal{K}_\beta &: [r_1, r_2, \phi_1, \phi_2] \mapsto [r_2, r_1, \phi_2 - 2m\beta, \phi_1 + 2m\beta]. \end{aligned} \tag{B3}$$

The action of $\mathcal{K}_0$ is simple, $\mathcal{K}_0 : [r_1, r_2, \phi_1, \phi_2] \mapsto [r_2, r_1, \phi_2, \phi_1]$. The integer m specifies the action of $O(2)$ on the bifurcating solution; it corresponds to the azimuthal wave number. The state Q_0 is $O(2)$ invariant, it is stable for $\mu < 0$ and unstable for $\mu > 0$. Q_1 and Q_2 are rotating waves, i.e., advancing in time is the same as applying a rotation:

$$\begin{aligned} \phi_1(t) &= \phi_1(0) + \omega t = \mathcal{R}_{\omega t/m}\, \phi_1(0), \\ \phi_2(t) &= \phi_2(0) - \omega t = \mathcal{R}_{-\omega t/m}\, \phi_2(0). \end{aligned} \tag{B4}$$

Therefore, $Q_1(t) = \mathcal{R}_{\omega t/m} Q_1(0)$ and $Q_2(t) = \mathcal{R}_{-\omega t/m} Q_2(0)$. Q_1 and Q_2 rotate in opposite senses, and $\mathcal{K}_0$ transforms one into the other, $\mathcal{K}_0\, Q_1 = Q_2$, so they are $\mathcal{K}_0$-conjugate states. Q_1 and Q_2 have a space-time symmetry consisting of simultaneously rotating and advancing in time, so as a set each orbit is $SO(2)$ invariant. Q_3 is $\mathcal{K}_0$-symmetric, $\mathcal{K}_0\, Q_3 = Q_3$. It is a superposition of the rotating waves Q_1 and Q_2; i.e., it is a standing wave. The analysis of the stability of the bifurcated solutions for $a > b$ gives that Q_1 and Q_2 are unstable and Q_3 is stable, whereas for $a < b$, Q_1 and Q_2 are stable and Q_3 is unstable. These results are summarized in the bifurcation diagram shown in Fig. 23, which also shows phase portraits before ($\mu < 0$) and after ($\mu > 0$) the bifurcation.

When the nondegeneracy conditions are not fulfilled, i.e., when some of the inequalities, $a \neq 0$ and $a \pm b \neq 0$, are close to equality, higher order terms must be included in the normal form resulting in additional bifurcations and solution branches near the Hopf bifurcation point. Golubitsky and Roberts [45] and Crawford and Knobloch [46] have analyzed in great detail all the possible additional bifurcation scenarios. Here, we only mention one of these, with $a \approx b$, that corresponds to the localized plume problem under consideration. In this case, the stability of the three bifurcating solutions is not easy to determine, and additional bifurcations take place when higher order terms are considered. Following Crawford and Knobloch [46], the normal form is now

$$\begin{aligned} \dot{r}_1 &= r_1\big[\mu - (1+\epsilon)r_1^2 - (1-\epsilon)r_2^2 - 2r_2^2\big(r_1^2 - r_2^2\big)\big], \\ \dot{r}_2 &= r_2\big[\mu - (1+\epsilon)r_2^2 - (1-\epsilon)r_1^2 + 2r_1^2\big(r_1^2 - r_2^2\big)\big], \end{aligned} \tag{B5}$$

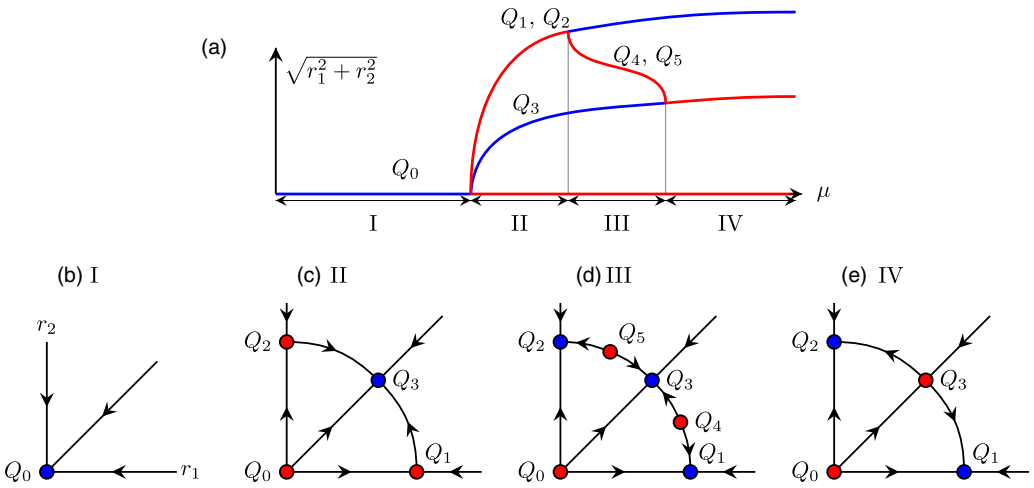

FIG. 24. (a) Bifurcation diagram of the degenerate Hopf bifurcation breaking $O(2)$ symmetry associated with the normal form (B5) and $a \approx b$. The blue (red) curves and symbols represent stable (unstable) solutions. The phase portraits over the ranges I–IV of μ are in panels (b–e).

where ϵ is a small but fixed positive parameter, and the fifth order terms are needed for the normal form to be persistent, i.e., so that the dynamics do not change qualitatively under arbitrary small perturbations of the equations. The bifurcation diagram and associated phase portraits are shown in Fig. 24. What is new in this configuration is that the stability properties of the rotating and standing wave branches of solutions are switched at some $\mu > 0$. This happens through a new family of two-tori solutions that bifurcate from Q_3 at a Z_2 symmetry-breaking bifurcation, spawning a pair of Z_2 conjugate two-tori states, Q_4 and Q_5, to lower μ (i.e., the Neimark–Sacker bifurcations are subcritical). The Q_4 and Q_5 solution branches terminate on Q_1 and Q_2 at supercritical Neimark–Sacker bifurcations rendering Q_1 and Q_2 stable for increasing μ. Over the range of μ in between the two Neimark–Sacker bifurcations, the Q_1, Q_2, and Q_3 are all stable. This hysteretic range of μ is $\epsilon(1-\epsilon) \leqslant \mu \leqslant \epsilon$, and the values of the amplitudes r_i of Q_4 and Q_5 are

$$r_1^2 = \tfrac{1}{2}(\epsilon \pm \sqrt{\epsilon - \mu}), \quad r_2^2 = \tfrac{1}{2}(\epsilon \mp \sqrt{\epsilon - \mu}), \tag{B6}$$

with the $+$ sign corresponding to Q_4 and the $-$ sign to Q_5.

So far, the discussion has been focused on the Hopf bifurcation of fixed points of an ordinary differential equation (ODE) that breaks $O(2)$ symmetry. In the localized plume problem under consideration, the first Hopf bifurcation preserves $O(2)$, resulting in the periodic puffing state P_0, and it is the second bifurcation that breaks $O(2)$ symmetry. The bifurcations of a periodic solution can be analyzed using a Poincaré section, so that the limit cycle P_0 becomes a fixed point of the Poincaré map. Crawford and Knobloch [42] have explored the symmetry-breaking bifurcations in maps with $O(2)$ symmetry, showing that all the results obtained for the ODE also apply to maps. In moving from the Poincaré map to the underlying partial differential equation (PDE) Navier–Stokes–Boussinesq system (1), Q_0 is the $O(2)$-invariant periodic puffing plume P_0, Q_1, and Q_2 are the quasiperiodic R_1, and Q_3 is the quasiperiodic K_1. The dynamics and stability properties are the same as in the ODE (B1) case, provided the nondegeneracy conditions ($a \neq 0$ and $a \pm b \neq 0$) are fulfilled and provided there are no resonances between the frequencies of the two-tori solution, which is precisely what happens in the plume problem under consideration. The bifurcation diagram for the degenerate Hopf bifurcation in Fig. 24 captures the dynamics near the Neimark–Sacker bifurcation of the puffing plume in the full system (1), shown in Fig. 5.

[1] P. F. Linden, Convection in the environment, in *Perspectives in Fluid Dynamics*, edited by G. K. Batchelor, H. K. Moffatt, and M. G. Worster (Cambridge University Press, Cambridge, UK, 2000), pp. 289–345.
[2] N. B. Kaye, Turbulent plumes in stratified environments: A review of recent work, Atmos.-Ocean **46**, 433 (2008).
[3] A. W. Woods, Turbulent plumes in nature, Annu. Rev. Fluid Mech. **42**, 391 (2010).
[4] B. R. Morton, G. Taylor, and J. S. Turner, Turbulent gravitational convection from maintained and instantaneous sources, Proc. R. Soc. London A **234**, 1 (1956).
[5] Z. He and Y. Lou, Integral model for multiple forced plumes arranged around a circle in a linearly stratified environment, Phys. Rev. Fluids **4**, 123501 (2019).
[6] H. Xiao, M. J. Gollner, and E. S. Oran, From fire whirls to blue whirls and combustion with reduced pollution, Proc. Natl. Acad. Sci. USA **113**, 9457 (2016).
[7] A. D. Weiss, P. Rajamanickam, W. Coenen, A. L. Sánchez, and F. A. Williams, A model for the constant-density boundary layer surrounding fire whirls, J. Fluid Mech. **900**, A22 (2020).
[8] F. Battaglia, R. G. Rehm, and H. R. Baum, The fluid mechanics of fire whirls: An inviscid model, Phys. Fluids **12**, 2859 (2000).
[9] F. C. Martins, J. M. C. Pereira, and J. C. F. Pereira, Vorticity transport in laminar steady rotating plumes, Phys. Fluids **32**, 043604 (2020).
[10] Y. Dai, A. Klimenko, Y. Lu, and K. Hooman, Asymptotic approximations for swirling turbulent plume rising from circular sources, Phys. Rev. Fluids **6**, 094604 (2021).
[11] A. Fabregat Tomàs, A. C. Poje, T. M. Özgökmen, and W. K. Dewar, Effects of rotation on turbulent buoyant plumes in stratified environments, J. Geophys. Res. Oceans **121**, 5397 (2016).
[12] B. R. Sutherland, Y. Ma, M. R. Flynn, D. Frank, P. F. Linden, D. Lemasquerier, M. Le Bars, C. Pacary, T. Jamin, T. Dauxois, and S. Joubaud, Plumes in rotating fluid and their transformation into tornados, J. Fluid Mech. **924**, A15 (2021).
[13] F. A. Williams, Scaling considerations for fire whirls, Progress Scale Modeling, An International J. **1**, 1 (2020).
[14] E. Ezhova, C. Cenedese, and L. Brandt, Dynamics of a turbulent buoyant plume in a stratified fluid: An idealized model of subglacial discharge in Greenland fjords, J. Phys. Oceanogr. **47**, 2611 (2017).
[15] J. D. Crawford and E. Knobloch, Symmetry and symmetry-breaking bifurcations in fluid dynamics, Annu. Rev. Fluid Mech. **23**, 341 (1991).
[16] B. M. Cetegen and K. D. Kasper, Experiments on the oscillatory behavior of buoyant plumes of helium and helium-air mixtures, Phys. Fluids **8**, 2974 (1996).
[17] X. Jiang and K. H. Luo, Direct numerical simulation of the puffing phenomenon of an axisymmetric thermal plume, Theor. Comput. Fluid Dyn. **14**, 55 (2000).
[18] F. Plourde, M. V. Pham, S. D. Kim, and S. Balachandar, Direct numerical simulations of a rapidly expanding thermal plume: structure and entrainment interaction, J. Fluid Mech. **604**, 99 (2008).
[19] K. K. Bharadwaj and D. Das, Global instability analysis and experiments on buoyant plumes, J. Fluid Mech. **832**, 97 (2017).
[20] P. Meunier and F. Nadal, From a steady plume to periodic puffs during confined carbon dioxide dissolution, J. Fluid Mech. **855**, 1 (2018).
[21] E. Khrapunov and Y. Chumakov, Structure of the natural convective flow above to the horizontal surface with localized heating, Int. J. Heat Mass Transf. **152**, 119492 (2020).
[22] S. Kimura and A. Bejan, Mechanism for transition to turbulence in buoyant plume flow, Int. J. Heat Mass Transf. **26**, 1515 (1983).
[23] H. Q. Yang, Buckling of a thermal plume, Int. J. Heat Mass Transf. **35**, 1527 (1992).
[24] T. Maxworthy, The flickering candle: Transition to a global oscillation in a thermal plume, J. Fluid Mech. **390**, 297 (1999).
[25] M. Qiao, Z. F. Tian, B. Nie, and F. Xu, The route to chaos for plumes from a top-open cylinder heated from underneath, Phys. Fluids **30**, 124102 (2018).
[26] T. Maxworthy, A vorticity source for large-scale dust devils and other comments on naturally occurring columnar vortices, J. Atmos. Sci. **30**, 1717 (1973).

[27] K. E. Torrance, Natural convection in thermally stratified enclosures with localized heating from below, J. Fluid Mech. **95**, 477 (1979).
[28] C. Dombrowski, B. Lewellyn, A. I. Pesci, J. M. Restrepo, J. O. Kessler, and R. E. Goldstein, Coiling, Entrainment, and Hydrodynamic Coupling of Decelerated Fluid Jets, Phys. Rev. Lett. **95**, 184501 (2005).
[29] R. V. K. Chakravarthy, L. Lesshaft, and P. Huerre, Local linear stability of laminar axisymmetric plumes, J. Fluid Mech. **780**, 344 (2015).
[30] K. E. Torrance, L. Orloff, and J. A. Rockett, Experiments on natural convection in enclosures with localized heating from below, J. Fluid Mech. **36**, 21 (1969).
[31] K. E. Torrance and J. A. Rockett, Numerical study of natural convection in an enclosure with localized heating from below—Creeping flow to the onset of laminar instability, J. Fluid Mech. **36**, 33 (1969).
[32] J. M. Lopez and F. Marques, Instability of plumes driven by localized heating, J. Fluid Mech. **736**, 616 (2013).
[33] F. Marques and J. M. Lopez, Spontaneous generation of a swirling plume in a stratified ambient, J. Fluid Mech. **761**, 443 (2014).
[34] J. K. Ansong and B. R. Sutherland, Internal gravity waves generated by convective plumes, J. Fluid Mech. **648**, 405 (2010).
[35] B. Fornberg, *A Practical Guide to Pseudospectral Methods* (Cambridge University Press, Cambridge, UK, 1998).
[36] A. P. Vincent, D. A. Yuen, D. Munger, and G. Zhu, On the dynamics of 3D single thermal plumes at various Prandtl numbers and Rayleigh numbers, Geophys. Astrophys. Fluid Dyn. **106**, 138 (2012).
[37] See Supplemental Material at http://link.aps.org/supplemental/10.1103/PhysRevFluids.8.023903 for additional information in the form of supplementary movies.
[38] Y. A. Kuznetsov, *Elements of Applied Bifurcation Theory*, 3rd ed. (Springer, Berlin, 2004).
[39] F. Marques and J. M. Lopez, Spatial and temporal resonances in a periodically forced extended system, Physica D **136**, 340 (2000).
[40] F. Marques and J. M. Lopez, Precession of a rapidly rotating cylinder flow: Traverse through resonance, J. Fluid Mech. **782**, 63 (2015).
[41] J. M. Lopez and F. Marques, Impact of centrifugal buoyancy on stratorotational instability, J. Fluid Mech. **890**, A9 (2020).
[42] J. D. Crawford and E. Knobloch, Symmetry-breaking bifurcations in $O(2)$ maps, Phys. Lett. A **128**, 327 (1988).
[43] P. Gutierrez-Castillo and J. M. Lopez, Nonlinear mode interactions in a counter-rotating split-cylinder flow, J. Fluid Mech. **816**, 719 (2017).
[44] E. Knobloch, Symmetry and instability in rotating hydrodynamic and magnetohydrodynamic flows, Phys. Fluids **8**, 1446 (1996).
[45] M. Golubitsky and M. Roberts, A classification of degenerate Hopf bifurcations with $O(2)$ symmetry, J. Diff. Eqn. **69**, 216 (1987).
[46] J. D. Crawford and E. Knobloch, Classification and unfolding of degenerate Hopf bifurcations with $O(2)$ symmetry: No distinguished parameter, Physica D **31**, 1 (1988).